The ^{197}Au(n,γ) cross section in the resonance region

C. Massimi,[1] C. Domingo-Pardo,[2,*] G. Vannini,[1] L. Audouin,[3] C. Guerrero,[4] U. Abbondanno,[5] G. Aerts,[6] H. Álvarez,[7] F. Álvarez-Velarde,[4] S. Andriamonje,[6] J. Andrzejewski,[8] P. Assimakopoulos†,[9] G. Badurek,[10] P. Baumann,[11] F. Bečvář,[12] F. Belloni,[5] E. Berthoumieux,[6] F. Calviño,[13] M. Calviani,[14] D. Cano-Ott,[4] R. Capote,[15,16] C. Carrapiço,[17,6] P. Cennini,[14] V. Chepel,[18] E. Chiaveri,[14] N. Colonna,[19] G. Cortes,[20] A. Couture,[21] J. Cox,[21] M. Dahlfors,[14] S. David,[3] I. Dillmann,[22] W. Dridi,[6] I. Duran,[7] C. Eleftheriadis,[23] L. Ferrant†,[3] A. Ferrari,[14] R. Ferreira-Marques,[18] K. Fujii,[5] W. Furman,[24] S. Galanopoulos,[25] I. F. Gonçalves,[17] E. González-Romero,[4] F. Gramegna,[26] F. Gunsing,[6] B. Haas,[27] R. Haight,[28] M. Heil,[22] A. Herrera-Martinez,[14] M. Igashira,[29] E. Jericha,[10] F. Käppeler,[22] Y. Kadi,[14] D. Karadimos,[9] D. Karamanis,[9] M. Kerveno,[11] P. Koehler,[30] E. Kossionides,[31] M. Krtička,[12] C. Lampoudis,[32] C. Lederer,[33] H. Leeb,[10] A. Lindote,[18] I. Lopes,[18] M. Lozano,[16] S. Lukic,[11] J. Marganiec,[8] S. Marrone,[19] T. Martínez,[4] P. Mastinu,[26] E. Mendoza,[4] A. Mengoni,[15,14] P.M. Milazzo,[5] C. Moreau,[5] M. Mosconi,[22] F. Neves,[18] H. Oberhummer,[10] S. O'Brien,[21] J. Pancin,[6] C. Papadopoulos,[25] C. Paradela,[7] A. Pavlik,[33] P. Pavlopoulos,[34] G.Perdikakis,[25] L. Perrot,[6] M. T. Pigni,[10] R. Plag,[22] A. Plompen,[32] A. Plukis,[6] A. Poch,[20] J. Praena,[26] C. Pretel,[20] J. Quesada,[16] T. Rauscher,[35] R. Reifarth,[28] M. Rosetti,[36] C. Rubbia,[14] G. Rudolf,[11] P. Rullhusen,[32] L. Sarchiapone,[14] R. Sarmento,[17] I. Savvidis,[23] C. Stephan,[3] G. Tagliente,[19] J. L. Tain,[37] L. Tassan-Got,[3] L. Tavora,[17] R. Terlizzi,[19] P. Vaz,[17] A. Ventura,[36] D. Villamarin,[4] V. Vlachoudis,[14] R. Vlastou,[25] F. Voss,[22] S. Walter,[22] M. Wiescher,[21] and K. Wisshak[22]

(The n_TOF Collaboration (www.cern.ch/ntof))

[1] *Dipartimento di Fisica, Università di Bologna, and Sezione INFN di Bologna, Italy*
[2] *GSI Helmholtzzentrum für Schwerionenforschung GmbH, Darmstadt, Germany*
[3] *Centre National de la Recherche Scientifique/IN2P3 - IPN, Orsay, France*
[4] *Centro de Investigaciones Energeticas Medioambientales y Tecnologicas, Madrid, Spain*
[5] *Istituto Nazionale di Fisica Nucleare, Trieste, Italy*
[6] *CEA/Saclay - IRFU, Gif-sur-Yvette, France*
[7] *Universidade de Santiago de Compostela, Spain*
[8] *University of Lodz, Lodz, Poland*
[9] *University of Ioannina, Greece*
[10] *Atominstitut der Österreichischen Universitäten, Technische Universität Wien, Austria*
[11] *Centre National de la Recherche Scientifique/IN2P3 - IReS, Strasbourg, France*
[12] *Faculty of Mathematics and Physics, Charles University, Prague, Czech Republic*
[13] *Universidad Politecnica de Madrid, Spain*
[14] *CERN, Geneva, Switzerland*
[15] *International Atomic Energy Agency (IAEA), Nuclear Data Section, Vienna, Austria*
[16] *Universidad de Sevilla, Spain*
[17] *Instituto Tecnológico e Nuclear - ITN, Lisbon, Portugal*
[18] *LIP - Coimbra & Departamento de Fisica da Universidade de Coimbra, Portugal*
[19] *Istituto Nazionale di Fisica Nucleare, Bari, Italy*
[20] *Universitat Politecnica de Catalunya, Barcelona, Spain*
[21] *University of Notre Dame, Notre Dame, USA*
[22] *Karlsruhe Institute of Technology, Institut für Kernphysik, Germany*
[23] *Aristotle University of Thessaloniki, Greece*
[24] *Joint Institute for Nuclear Research, Frank Laboratory of Neutron Physics, Dubna, Russia*
[25] *National Technical University of Athens, Greece*
[26] *Istituto Nazionale di Fisica Nucleare, Laboratori Nazionali di Legnaro, Italy*
[27] *Centre National de la Recherche Scientifique/IN2P3 - CENBG, Bordeaux, France*
[28] *Los Alamos National Laboratory, New Mexico, USA*
[29] *Tokyo Institute of Technology, Tokyo, Japan*
[30] *Oak Ridge National Laboratory, Physics Division, Oak Ridge, USA*
[31] *NCSR, Athens, Greece*
[32] *EC-JRC-IRMM, Geel, Belgium*
[33] *Faculty of Physics, University of Vienna, Austria*
[34] *Pôle Universitaire Léonard de Vinci, Paris La Défense, France*
[35] *Department of Physics - University of Basel, Switzerland*
[36] *ENEA, Bologna, Italy*
[37] *Instituto de Física Corpuscular, CSIC-Universidad de Valencia, Spain*

The (n,γ) cross section of ^{197}Au has been measured at n_TOF in the resolved resonance region, up to 5 keV, with the aim of improving the accuracy in an energy range where it is not yet considered standard. The measurements were performed with two different experimental setup and detection

techniques, the total energy method based on C_6D_6 detectors and the total absorption calorimetry based on a 4π BaF_2 array. By comparing the data collected with the two techniques, two accurate sets of neutron capture yields have been obtained, which could be the basis for a new evaluation leading to an extended cross section standard. An overall good agreement is found between the n_TOF results and evaluated cross sections with some significant exceptions for small resonances. A few resonances not included in the existing databases have also been observed.

I. INTRODUCTION

The main objectives of the experimental activity of the neutron time-of-flight facility, n_TOF, at CERN, are accurate measurements of neutron cross sections related to nuclear astrophysics [1, 2] and the collection of nuclear data related to emerging nuclear technologies for energy production and nuclear waste transmutation [3, 4, 5].

Most neutron cross-sections are measured relative to cross-section standards [6] for normalization to absolute values. So far, the ^{197}Au(n,γ) reaction at thermal energy and between 0.2 and 2.5 MeV is the only capture standard and most neutron capture cross section measurements refer to one or both energy regions. An alternative to the use of cross-section standards is the saturated resonance technique [7] using a low-energy saturated resonance, like for example the 4.9 eV resonance in ^{197}Au(n,γ) reaction. Due to its high capture cross section value, this resonance is saturated for a sample thickness greater than 30 μm.

Because of the convenient neutron induced radioactivity, chemical and isotopic purity, large thermal neutron capture and resonance capture integral, the Au capture cross section is of great importance, e. g. for flux measurements in nuclear reactors, in accelerator mass spectrometry as well as in neutron activation analysis.

The ^{197}Au(n,γ) cross section is not very accurately known in the resolved resonance region (RRR). The few previous measurements were carried out with liquid scintillation detectors containing H or F and did not cover the full RRR up to $\approx$ 5 keV. Resonance parameters up to 1 keV were determined in Refs. [8, 9, 10] by combining the results of different types of neutron cross section measurements (i. e. transmission through thick and thin samples, capture, self-indication and elastic scattering) and using the so-called area analysis [11]. From the resonance shape analysis of a transmission measurement Alves *et al.* [12] determined resonance parameters from 1 keV up to 2.5 keV. In the energy region 2.5-5 keV capture data from Macklin *et al.* [13] were combined with differential elastic scattering data from Hoffman *et al.* [14].

The evaluated cross sections in the neutron reaction libraries ENDF/B-VI [15] and ENDF/B-VII [16] (the latter based on the compilation of Ref. [17]) show small discrepancies. In addition, a few resonances reported by Desjardins *et al.* [8] and Julien *et al.* [10] are only partly included.

This situation motivated a new measurement of the capture cross section of ^{197}Au at the n_TOF facility with the aim of establishing the Au capture standard also in the energy range below 200 keV. To reduce systematic uncertainties as far as possible, the measurement was carried out with different gold samples and by using two independent detection techniques based on a total absorption calorimeter (TAC) and a pair of C_6D_6 detectors (Sec. II).

This paper presents the results of a resonance shape analysis with the R-matrix code SAMMY [18] for the resolved resonances in the energy region between 1 eV and 5 keV. The analysis procedure for the TAC and C_6D_6 data is illustrated in Secs. III and IV, respectively. The comparison of the two data sets with each other and with evaluated cross section data is given in Sec. V.

The unresolved resonance region between 5 keV and 1 MeV is being analyzed in parallel and will be published separately [19].

II. MEASUREMENTS

A. The n_TOF facility

During Phase-I of the n_TOF facility (2001-2004) the neutron beam was produced by spallation induced by a 20 GeV/c proton beam, with up to 7×10^{12} particles per pulse, impinging on a $80\times80\times60$ cm^3 lead target with a repetition rate of 0.4 Hz. These characteristic features of n_TOF allows one

- to cover the neutron energy interval from 1 eV up to 250 MeV in a single run,
- to achieve an extremely high instantaneous neutron flux, and
- to prevent pulse overlap even for sub-thermal neutrons.

A 5.8 cm thick water layer surrounding the lead target serves as coolant and as a moderator of the initially fast neutron spectrum, providing a wide neutron energy spectrum with a nearly $1/E_n$ isolethargic flux dependence in the neutron energy region from 1 eV to 1 MeV. An evacuated beam line leads to the experimental area at a distance of 185 m from the lead target. The neutron beam line is extended for an additional 12 m beyond the experimental area to minimize the background from back-scattered neutrons. A full description of the characteristics and performance of the facility can be found in Refs. [20, 21, 22].

*corresponding author: c.domingopardo@gsi.de

The neutron beam is shaped by two collimators at 135 and 175 m from the spallation target. For capture measurements, the second collimator is used with an inner diameter of 1.8 cm, resulting in a nearly symmetric Gaussian-shaped beam profile at the sample position with a standard deviation of about 0.77 cm at low neutron energies [23]. The neutron energy is determined via time-of-flight (TOF), using the γ-flash from the impact of the proton pulse on the spallation target as the time reference.

The relationship for converting TOF into neutron energy was accurately verified in the energy range from 1 eV up to ∼1 MeV by means of specific capture resonances in ^{32}S, ^{193}Ir and ^{238}U, which are accepted energy standards [24]. For each detector signal the corresponding TOF is determined on an event-by-event basis with an accuracy of about 2 ns.

The data acquisition system (DAQ) [25] with 54 channels consists of high frequency flash analog-to-digital converters (FADC) [26]. Each channel has an 8 Mbyte memory buffer, and is operated at a rate of 500 Msamples/s. In combination with the low duty-cycle, the DAQ allows one to record the full sequence of signals in each detector in a TOF interval from relativistic neutron energies down to approximately 1 eV. This operation mode corresponds to a zero dead-time data acquisition that is important for avoiding large dead-time corrections at low neutron energies, where the (n,γ) cross section of Au is rather large. After zero suppression the data are reduced and stored in the CERN central data recording system. Especially designed pulse shape analysis routines are used in the data reduction stage to extract amplitude, integrated slow and fast component, and TOF from the digitized detector signals. This information together with the corresponding detector number and the number of protons in the respective pulse are then used for further data analysis. For more details see Ref. [25].

B. Neutron capture detectors

Neutron capture events are characterized by γ-ray cascades leading from the excited state to the ground state of the compound nucleus formed in the reaction. In the n_TOF measurements, a total energy detection system with two C_6D_6 liquid scintillation detectors as well as a total γ-ray absorption calorimeter (TAC) have been used for measurements of capture cross sections. These two techniques are briefly described in the following.

A first set of measurements was carried out using two C_6D_6 detectors, which have been especially designed [27] with the aim of reducing the γ-ray background induced by neutrons scattered in the sample and captured in or near the detectors. As illustrated in Refs. [28, 29] this background has been recognized as a relevant source of error in previous measurements. Recorded events in the C_6D_6 detectors need to be treated by the pulse height weighting technique [30] to achieve the proper energy-dependence of the γ-ray efficiency as described in more detail in Sec. IV.

The n_TOF TAC [31, 32, 33, 34, 35] is a 4π detector with nearly 100% detection efficiency for capture γ-ray cascades and an energy resolution of 15% at 662 keV and of 6% at 6.1 MeV. It consists of 40 BaF_2 crystals contained in ^{10}B loaded carbon fiber capsules forming a spherical shell 15 cm in thickness and with an inner diameter of 20 cm. Neutrons scattered from the sample in the center of the TAC are moderated and partly absorbed in a 5 cm thick spherical shell made of $C_{12}H_{20}O_4(^6Li)_2$ surrounding the sample.

The TAC is ideal for capture measurements of low mass samples, as well as of radioactive and fissile isotopes, due to its very high total efficiency and because it allows one to select capture reactions via the total energy of the γ-ray cascade and to reject events due to other processes, in particular in-beam γ-rays from neutron captures in the water moderator of the spallation target. A certain drawback of the device is the relatively high neutron sensitivity, mostly due to capture of scattered neutrons in the Ba isotopes of the scintillator (Sec. III B 2). To some extent this problem has been reduced by means of the absorber shell around the sample and the ^{10}B-loaded carbon fiber capsules. Contrary to the TAC, the C_6D_6 setup is optimized for cases where the total cross section is strongly dominated by the elastic channel. These detectors are in fact characterized by a very low neutron sensitivity of about 10^{-4}, two orders of magnitude smaller than that of the TAC, thus providing reliable results even for very small Γ_γ/Γ_n ratios.

The setup for the capture measurements is complemented by the silicon flux monitor (SiMon) [36], which consists of a thin ^{6}Li deposit on a thin Mylar foil surrounded by a set of four silicon detectors outside the neutron beam for recording the tritons and α particles from the $^6Li(n,\alpha)^3H$ reaction.

C. Samples

Gold samples, which differed in size and thickness, were used in the measurements to control sample-related systematic effects. The characteristics of the samples are listed in Tab. I. In addition to gold, samples of ^{nat}C and ^{nat}Pb of the same diameter as the Au samples have been used to evaluate the background due to sample scattered neutrons and in-beam γ-rays.

Table I: Gold samples for the two capture measurements.

	TAC	C_6D_6
Diameter (cm)	1.0	2.205
Mass (g)	0.1854	1.871
Thickness (cm)	1.22×10^{-2}	2.5×10^{-2}
Areal density (at/barn)	7.3×10^{-4}	1.498×10^{-3}

III. ANALYSIS OF THE TAC DATA

The energy calibration of each individual BaF_2 crystal was obtained by means of standard γ-ray sources, i. e. ^{137}Cs (662 keV), ^{88}Y (898 and 1836 keV), and Pu/C (6131 keV from ^{16}O). The energy resolution of each BaF_2 module and of the entire array were obtained from these measurements as well.

A. From measured count rate to capture yield

The processed information from the 40 BaF_2 crystals is combined off-line in a so-called calorimetric routine with the aim of identifying capture events. Although the time resolution of each crystal is less than 2 ns due to the very fast decay time of the BaF_2 scintillators, the overall time resolution of the TAC is larger (i. e. 26 ns) due to the uncertainty in the calibration and synchronization of the different FADCs. Therefore, the condition that defines an event in the TAC is the recording of signals in two or more crystals within a coincidence window of 26 ns.

A 150 keV threshold is used for the individual signals to reject electronic noise and to minimize pile-up effects (see Sec. III B 1). For each processed event, the calorimetric routine returns the total energy deposited in the TAC ($E_{\rm TAC}$), the incoming neutron energy ($E_{\rm n}$), and M_γ, the number of BaF_2 crystals in which a γ-ray is detected above threshold. The segmentation of the TAC is enough to ensure a close correlation between the multiplicity of the detected event and the number of γ-rays emitted in the capture cascade.

The probability that a capture reaction occurs in the sample is the capture yield, i. e. that fraction of neutron beam which undergoes a capture reaction in the sample. Experimentally it is obtained from the ratio of the total counts detected by the TAC, $C_{\rm Au}(E_{\rm n})$, and the incoming neutron fluence $\Phi(E_{\rm n})$ integrated over the beam profile,

$$Y_{\rm exp}(E_{\rm n}) = \frac{C_{\rm Au}(E_{\rm n}) - C_{\rm empty}(E_{\rm n})}{\epsilon \cdot f \cdot \Phi(E_{\rm n})}, \qquad (1)$$

in this expression, $C_{\rm empty}(E_{\rm n})$ are the counts measured without the sample, and represents the sample-independent background (other sources of background are discussed later), ϵ is the TAC efficiency for detecting a capture event, and f is the fraction of the neutron beam intercepting the sample.

The correction factors ϵ and f are independent of neutron energy in the range considered here. The efficiency ϵ depends on the conditions of the analysis, i. e. on the multiplicity window and the energy cuts chosen for the TAC response. The fact that the neutron beam profile varies very slightly with neutron energy was also properly taken into account.

Since the absolute normalization in our analysis is obtained via the 4.9 eV saturated resonance, it is not necessary to know the absolute value of the flux, but only the relative energy dependence of the neutron flux up to few keV, which has been measured with a ^{235}U parallel plate fission ionization chamber of PTB Braunschweig, Germany [37]. At neutron energies below 1 keV, we used the flux from the SiMon, which was normalized to the former data in the overlapping energy region.

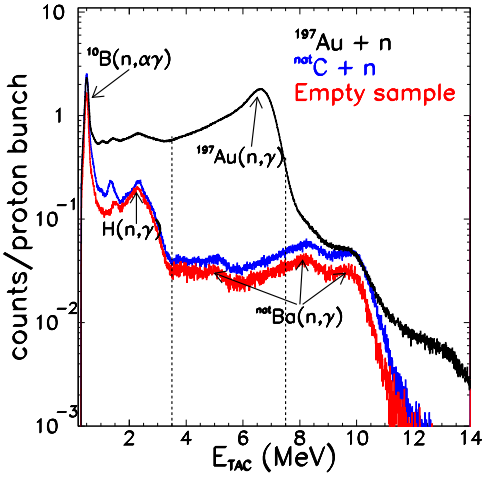

Figure 1: (Color online) The spectra of the energy deposited in the TAC measured with the Au and C samples compared to the case without sample (empty) in the neutron energy range $1 < E_{\rm n} < 5000$ eV. The adopted thresholds for the deposited energy are indicated by dashed vertical lines.

After the normalization factor N was determined via the 4.9 eV resonance, the experimental capture yield is

$$Y_{\rm exp}(E_{\rm n}) = N \cdot \frac{C_{\rm Au}(E_{\rm n}) - C_{\rm empty}(E_{\rm n})}{\Phi(E_{\rm n})}. \qquad (2)$$

Fig. 1 shows the total energy deposited in the TAC for the samples used in the measurement. The peak at 6.5 MeV corresponding to the excitation energy of the compound nucleus formed after a neutron capture on ^{197}Au is clearly visible. Moreover, background components are also present. A delicate part of the data analysis consists in the choice of the optimal thresholds for the deposited energy $E_{\rm TAC}$ to maximize the capture-to-background ratio.

The selection criteria in the present analysis are illustrated in Figs. 1 and 2. The adopted conditions are $3.5 < E_{\rm TAC} < 7.5$ MeV on the total deposited energy and $M_\gamma \geq 2$. As shown later, the choice for $E_{\rm TAC}$ minimizes the neutron sensitivity, since it allows us to reject the 2.2 MeV γ-rays produced by hydrogen capture in the absorber around the sample completely and neutron captures by the Ba isotopes in the crystals partly (in particular from the odd nuclei ^{135,137}Ba, which are characterized by capture energies above 7 MeV). As a further advantage pile-up of two consecutive capture cascades, which mimics events with large total energy deposition, is reduced (Sec. III B 1). Although the overall efficiency de-

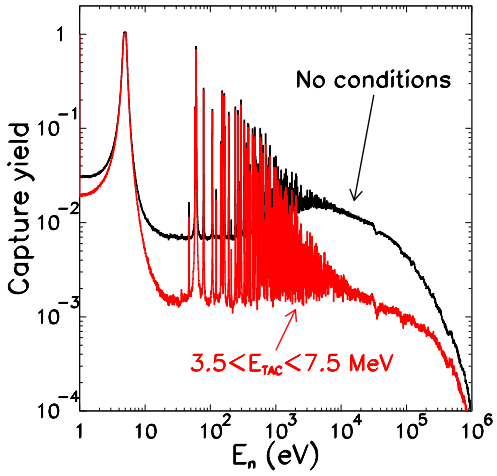

Figure 2: (Color online) Experimental capture yields for the ^{197}Au(n,γ) reaction extracted with and without the selection criteria for the deposited energy $E_{\rm TAC}$.

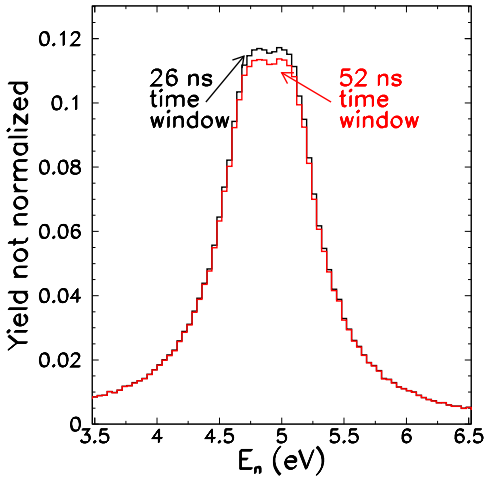

Figure 3: (Color online) Capture yields extracted with coincidence time windows of 26 and 52 ns to illustrate the detector dead-time at the example of the first Au resonance at 4.9 eV. In the present analysis a time window of 26 ns was adopted.

creased to 60% by these conditions, the resulting signal-to-background ratio is drastically improved, as shown in Fig. 2.

B. Corrections and background evaluation

The capture yield measured with the TAC must be corrected for systematic effects, before performing a resonance analysis with an R-Matrix code. The corrections are related to the dead-time of the detector setup and to its neutron sensitivity.

1. Pile-up and dead-time

The large counting rate associated with the very high instantaneous neutron flux at n_TOF results in two different effects that have to be considered in the analysis of the TAC data, i. e. pile-up of consecutive signals in each BaF_2 crystal and the occurrence of two consecutive capture events within the 26 ns coincidence window used in the calorimetric routine. In analogy to standard electronics, we will refer to this second effect as detector dead-time. In principle, the n_TOF DAQ should not be affected by pile-up because the FADCs allow one to identify and to reconstruct two consecutive signals (see for example Ref. [38]), contrary to standard electronics and acquisition systems. However, a correction is still required if two signals are too close in time to be correctly identified by the reconstruction routine [31], especially if a small signal occurs on the tail of a preceding larger signal. In this way, a fraction of low-energy γ-rays may be lost, thus distorting primarily the multiplicity and, to a lesser extent, the total energy deposited in the TAC.

The corresponding correction is based on the exact signal shape of each crystal and on the ability of the reconstruction routine to identify pile-up events. One possibility is to rely on detailed simulations of the detector response as shown in Ref. [31]. Another approach, which has been adopted in the present study, takes advantage of the fact that the n_TOF proton beam is delivered in two different modes, a dedicated mode with an intensity of 7×10^{12} protons/pulse and a parasitic mode with approximately half the intensity. The comparison between data collected in both modes reveals that pile-up problems are affecting only the low-energy part of the energy deposited in each crystal. Therefore, the pile-up effect is reduced to a negligible level by an energy threshold of 150 keV for the individual crystals and by the multiplicity condition ($M_\gamma \geq 2$).

The second, more important effect of the high counting rate at n_TOF is related to the occurrence of two capture events within the coincidence window used in the calorimetric routine to sum-up all γ-rays belonging to a capture event.

For the largest observed counting rates (in the range 1-3 counts/μs), the probability of detecting two capture events in the coincidence window can not be neglected. As shown in Fig. 3 an increase of the time window from 26 to 52 ns results in a reduction of the capture yield (obtained with the present analysis conditions on $E_{\rm TAC}$ and M_γ). Due to the constraints on total deposited energy, the combination of two (or more) capture reactions leads to the loss of one or both events, depending on whether the resulting $E_{\rm TAC}$ falls within the adopted pulse height window of $3.5 < E_{\rm TAC} < 7.5$ MeV. The effect is analogous to the loss of counts due to the dead-time in standard data processing and acquisition systems. There-

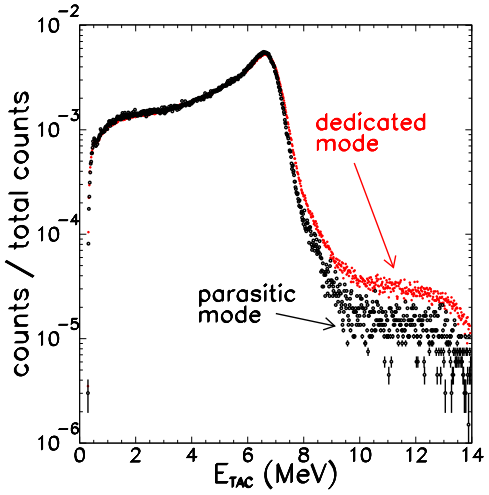

Figure 4: (Color online) The E_{TAC} spectra of ^{197}Au for parasitic and dedicated operation mode for capture events around the 4.9 eV resonance.

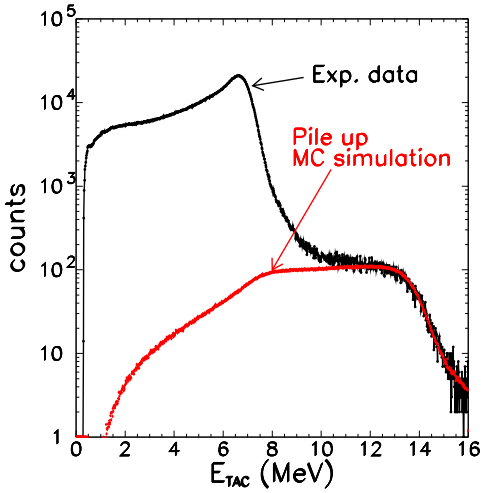

Figure 5: (Color online) Experimental distribution of the energy deposited in the TAC for neutron capture events around the 4.9 eV resonance in Au, and a Monte Carlo simulation of the pile-up effect for capture events taken from the same distribution.

fore, the counting rate for this detector dead-time has been corrected in first order by means of the standard non-cumulative (non-paralyzable) model (see for example Ref. [39]) with a dead time corresponding to the width of the coincidence window.

The E_{TAC} spectra in parasitic and dedicated mode for the TOF region around the resonance at 4.9 eV are compared in Fig. 4. Pile-up at the higher count rate in dedicated mode is clearly visible by the enhancement beyond 9 MeV.

The standard assumption that out of two or more coincident events only one is detected represents a first order correction. For the calorimetric method, however, other cases should be considered as well. With the conditions selected for E_{TAC} and M_γ, both events can be lost if the sum falls outside the limits of the total deposited energy. On the other hand, some events, which were lost for dead-time, would have been lost anyway, because they did not match the analysis conditions initially. The true number of lost events was estimated by means of the Monte Carlo (MC) method. In the simulation two events were randomly chosen from the measured E_{TAC} spectrum and added together. The resulting spectrum is shown in Fig. 5 together with the experimental E_{TAC} distribution. The second-order correction was determined by simulations of pile-up events. In particular, we have calculated the probability that pile-up events fulfill the analysis conditions for two randomly-chosen events from the experimental distribution. To avoid the background from sample-scattered neutrons in the E_{TAC} spectrum, the simulation was performed in the energy range between 4.8 and 5.1 eV. It was found that the resulting probability for pile-up corresponds on average to a 20% increase of the dead-time correction.

Accordingly, the counting rate was corrected by the following expression:

$$C_r' = C_r \frac{1 + C_r\tau(F_2 - 1)}{1 - C_r\tau}, \qquad (3)$$

where C_r' and C_r are the corrected and recorded count rates, τ is the dead time (i. e. 26 ns), and F_2 is the second order correction (1.2 on average). The main uncertainty of the dead time correction is caused by the second order correction, which was estimated to be of the order of 20%, leading to a maximum uncertainty of 1.5% in the corrected count rate.

The total correction at the top of the strongest resonances and for dedicated beam pulses is always less than 6%. Although small, the dead-time effect is distorting the resonance shape and can hamper the resonance analysis. On the flat top of the 4.9 eV resonance, for example, this distortion is about 2%. Therefore, a corresponding correction was always applied.

As a final remark, the structure between 12 and 14 MeV in the E_{TAC} spectrum of Fig. 1 is now explained by the pile-up feature in Fig. 5.

After the dead-time correction, a systematic check was carried out by comparing parasitic and dedicated pulses. Except for the 60.3 eV resonance, which shows the largest counting rate of $> 1\mu\mathrm{s}^{-1}$ with a corresponding dead time correction of 6%, the difference between the yields extracted for the two proton beam modes was found to be less than 1% as illustrated in Fig. 6, thus providing confidence in the validity of the dead-time correction.

2. *Background*

The background components, which result from

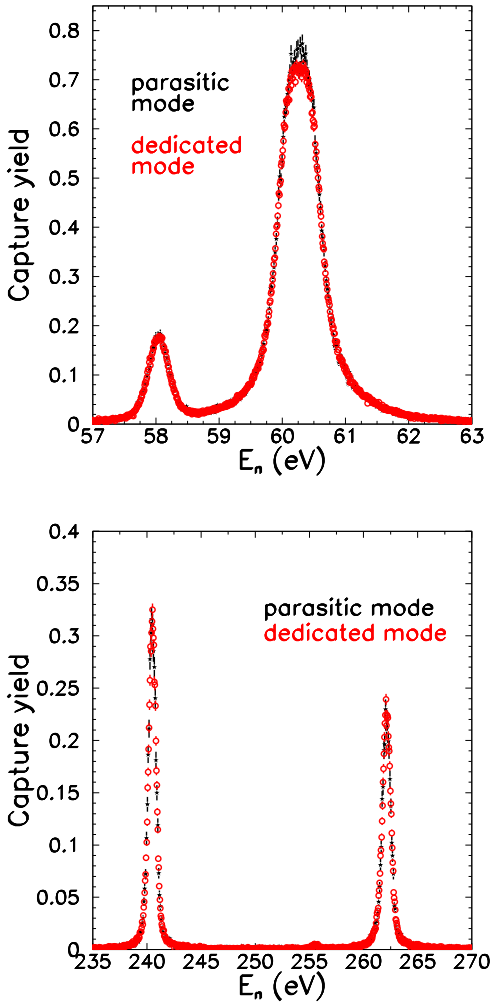

Figure 6: (Color online) Capture yields from data obtained in parasitic and dedicated beam mode for resonances with the largest dead time corrections.

- in-beam γ-rays;
- ambient background;
- α radioactivity of Ra contaminants in the scintillator [40].

were studied by means of dedicated measurements and have been reduced by the conditions on $E_{\rm TAC}$ discussed before and by pulse shape discrimination of the BaF_2 signals.

Another background component is due to sample-scattered neutrons. Scattered neutrons can be captured inside the TAC, mainly by the Ba isotopes of the scintillator, and may contaminate the capture yield from the Au sample. This background depends on the neutron sensitivity of the detector [41, 42], which can be defined as the ratio between the efficiencies for detecting scattered neutrons, ϵ_n, and capture events, ϵ_γ. This background causes an artificial increase of the resonance area, particularly in resonances where the neutron width exceeds the radiative width.

In Fig. 7 the capture yield of the ^{197}Au sample is compared with the yields from background runs with $^{\rm nat}$C, $^{\rm nat}$Pb, and without sample, which were all obtained with the analysis conditions described above. The Pb measurement provides a good estimate of the sample-dependent component of the backgound in the Au measurement, being the areal density, the atomic number and the non-resonant elastic cross section of the two samples comparable. Because of the very similar shape of Pb and C yields one can conclude that the background due to in-beam γ-rays is small. Moreover, the Pb and C yields are close to the yield obtained without sample, demonstrating the low level of the residual background, which is mainly due to the neutron sensitivity of the detector.

Several methods have been proposed to determine this background component [43, 44]. In the present analysis the neutron sensitivity was determined from a measurement with a thick graphite sample. In this case the measured count rates are weighted by the ratio of the capture and elastic cross sections of Au and C, respectively,

$$\frac{\epsilon_n}{\epsilon_\gamma} = \frac{C_{\rm C}}{C_{\rm Au}} \frac{Y_\gamma^{\rm Au}}{Y_n^{\rm C}}, \qquad (4)$$

where $C_{\rm C}$ and $C_{\rm Au}$ are the background corrected number of counts as a function of neutron energy. The capture yield for ^{197}Au and the one for elastic scattering for ^{12}C are calculated from the evaluated cross-sections in the ENDF/B-VI library[45].

As shown in Fig. 8 the neutron sensitivity of the 4π BaF_2 detector is about 0.1, three orders of magnitude higher than that of the n_TOF C_6D_6 setup [27]. However, the background due to scattered neutrons can be reduced in an efficient way by suitable conditions on the total deposited energy $E_{\rm TAC}$.

The optimal condition can be derived from the distributions of the total deposited energy shown in Fig. 1 for Au, C, and an empty sample. Apart from the peak at 6.5 MeV related to ^{197}Au(n,γ) reactions, structures at low energies are observed at 478 keV and 2.2 MeV associated with capture of scattered neutrons in the ^{10}B capsules and in the hydrogen contained in the inner shell of absorbing material. The structure above 7.5 MeV is caused by capture of scattered neutrons by the odd Ba isotopes of the scintillator. The remaining background components falling within the selected window for the deposited energy are due to capture reactions on ^{19}F and on the even Ba isotopes. However, these components are less evident in the $E_{\rm TAC}$ spectrum of Fig. 1 due to the low capture cross sections and/or low natural abundances of these isotopes. The main contributions to the neutron sensitivity are summarized in Table II.

The calculated neutron sensitivity is shown in Fig. 8 for different conditions on $E_{\rm TAC}$ and event multiplicity. The strongest reduction of about one order of magnitude

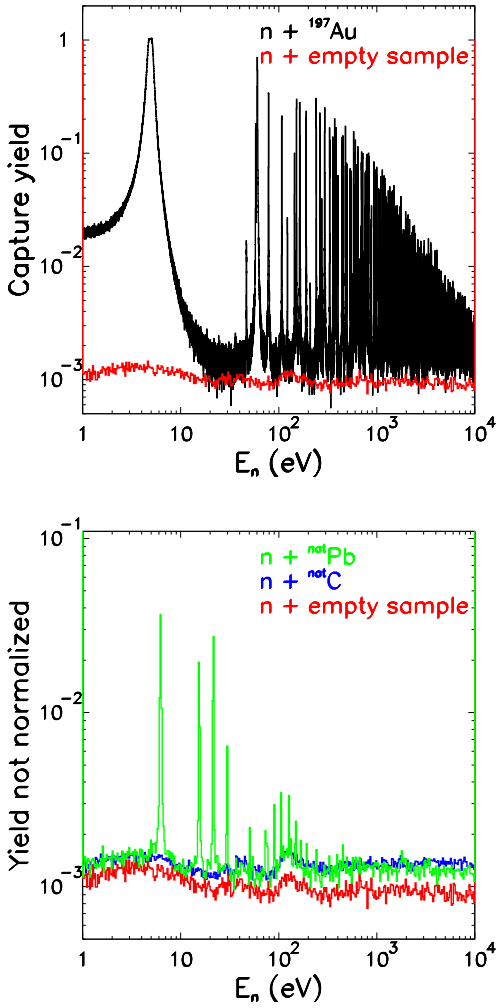

Figure 7: (Color online) Top: Experimental capture yield measured with Au and without sample. Bottom: Experimental yields measured without sample and with the ^{nat}C and ^{nat}Pb samples, all analyzed with the same conditions for energy deposition and multiplicity. Resonances in the ^{nat}Pb yield are due to a small Sb contamination.

is obtained with the condition used in the present analysis, i. e. $3.5 < E_{\rm TAC} < 7.5$ MeV and $M_\gamma \geq 2$, by which events related to neutron capture in the ^{10}B-loaded capsules as well as in the neutron absorber are rejected. The remaining background due to scattered neutrons is illustrated in Fig. 1 by the difference between the spectra taken with the C sample and that of the empty sample position.

For most resonances, this unavoidable background results in an increase of the neutron yield of a few percent, although it may reach up to 20% for resonances with very large Γ_n values. Therefore, a second step is needed in the analysis to subtract this residual background, either on the basis of resonance parameters from literature or directly from the present experimental data. In the

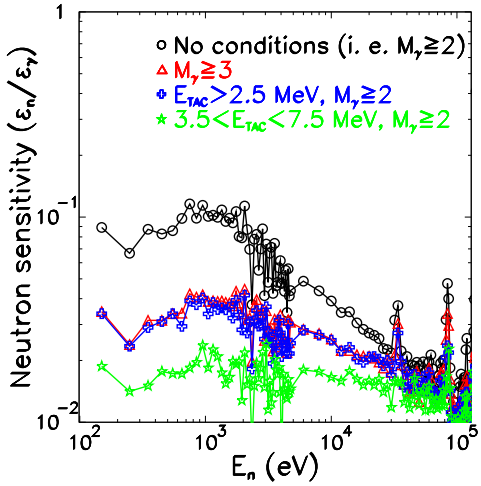

Figure 8: (Color online) The neutron sensitivity of the n_TOF TAC as a function of neutron energy for different conditions.

Table II: Main contributions to the neutron sensitivity of the TAC.

Isotope	Reaction	Energy (MeV)	Origin
^{10}B	$(n,\alpha\gamma)$	0.48	capsules
^{1}H	(n,γ)	2.2	n-absorber
^{138}Ba	(n,γ)	4.8	scintillator
^{137}Ba	(n,γ)	8.6	scintillator
^{135}Ba	(n,γ)	9.1	scintillator

first case, the neutron background B_n can be derived by scaling the measured carbon yield,

$$B_n = (Y_{\rm C} - Y_{\rm empty}) \frac{Y_n^{\rm Au}}{Y_n^{\rm C}} \qquad (5)$$

where $Y_n^{\rm Au}$ and $Y_n^{\rm C}$ are the elastic yields for Au and C from the evaluated ENDF/B-VI cross sections. The second method is described in more detail in Ref. [46] and relies exclusively on the measured $E_{\rm TAC}$ spectra. In this case, the residual background in the Au sample is determined from the spectra measured with the Au and C sample (subtracted for the spectrum without sample), which are scaled to match the tail of the $E_{\rm TAC}$ spectrum above 7.5 MeV (Fig. 9). This method relies on the assumption that only neutron capture on the odd Ba isotopes contributes above 7.5 MeV. Both techniques do have problems, however. The first method may suffer from the lack of reliable neutron widths in literature. It also tends to overestimate the background under the resonances, because multiple scattering in the absorber and in the BaF_2 scintillators distributes the corresponding background component over a larger TOF region beyond the resonance itself. Therefore, this method provides only an upper limit for the background. The second method may overestimate the background for the largest

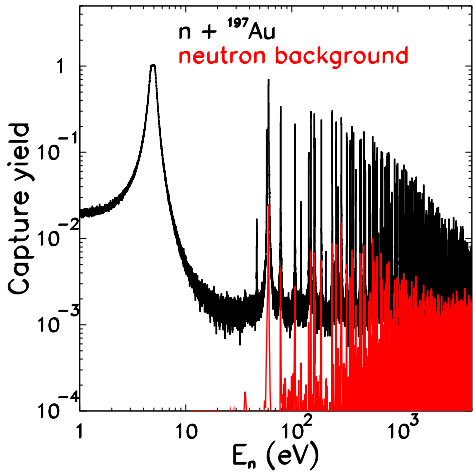

Figure 9: (Color online) Au capture yield and neutron background determined from experimental data using the second method described in the text.

resonances, since the $E_{\rm TAC}$ region above 7.5 MeV can be affected by pile-up events (see Figs. 5 and 9).

In the present analysis, the neutron background was determined by means of the second method using data obtained in parasitic mode, which are characterized by lower pile-up. The resulting background was verified and confirmed by the results calculated via Eq. 5. An example of the residual neutron background is given in Fig. 9.

This background and the associated statistical uncertainty are used as input in SAMMY code to analyze the experimental yields in terms of the R-matrix formalism. In this program the net capture yield

$$Y_\gamma(E_n) = Y_{\rm exp}(E_n) - Y_{bkg}(E_n). \quad (6)$$

is determined by linear interpolation of the background. Therefore, the uncertainties of this background are directly reflected in the uncertainties of the resonance parameters from the TAC data given in Table IV.

IV. ANALYSIS OF THE C_6D_6 DATA

A. From measured count rate to capture yield

The experimental yield is obtained as a function of neutron energy E_n from the weighted count rate N^w as [25, 47]:

$$Y_{\rm exp} = f_{\rm N} f_{\rm exp} \frac{N^w}{\Phi E_c}. \quad (7)$$

where $Y_{\rm exp}$, N^w, and Φ depend on TOF or the neutron energy (for sake of clarity this dependence is omitted in Eq. 7). The weighting of the detector signals and the determination of N^w is described below. $\Phi(E_n)$ is proportional to the total number of neutrons intersecting the sample with energy E_n measured with the SiMon detector [36], and the flux calibration is contained in the yield normalization factor $f_{\rm N}$. The yield correction factor $f_{\rm exp}$ accounts mostly for the 200 keV pulse height threshold in the γ-ray detectors (Sec. IV C). E_c denotes the total capture energy, which for a resonance at energy $E_{\rm R}$ is given by $E_c = S_n + E_{\rm R}$, where $S_n = 6.512$ MeV is the neutron separation energy of ^{197}Au.

The yield given by Eq. 7 still contains the contributions from capture and background events. The energy dependent background level $Y_{bkg}(E_n)$ is determined from complementary measurements as described in Sec. IV D. Finally, the net capture yield $Y_\gamma(E_n)$ is obtained by subtraction of the background as in Eq. 6.

B. Pulse height weighting technique

The pulse height weighting technique (PHWT) was introduced by Macklin and Gibbons [30] more than 40 years ago. By this technique the detector response is weighted in such a way that the detection efficiency becomes proportional to the energy of the registered γ-ray.

Before the first (n,γ) measurements at n_TOF, there was no common recipe for determining the corresponding weighting factors (WF) but different prescriptions have been used (see Refs. [48, 49] for example). Furthermore, the WFs applied in the first decades of the PHWT had typical uncertainties of 20% [50]. Therefore, a substantial effort was dedicated at n_TOF to validate the PHWT experimentally and to define a clear procedure to determine accurate WFs and the systematic uncertainty that can be achieved with this technique. It was shown that an uncertainty of better than 2% can be ascribed to the PHWT provided that realistic MC simulations of the experimental setup and of the capture events are included in the analysis [25]. At present, there is general agreement that the MC approach represents the correct method for the calculation of the WFs [25, 42, 51, 52].

1. *Determination of the WF*

The WFs for the present measurement were obtained from the response functions for monoenergetic γ-rays, which were calculated by means of detailed MC simulations of our experimental setup with GEANT4 [53]. The 3D spatial distribution of primary γ-ray events is generated using the neutron beam profile for the radial dimension [23] and the neutron absorption probability across the sample thickness, which obviously depends on the particular value of the cross section and, therefore, on neutron energy. In this way, the self-absorption effect of the γ-rays in the sample is realistically considered. This is the same approach as reported in previous works [25, 42, 47, 54, 55, 56, 57]. The slight energy

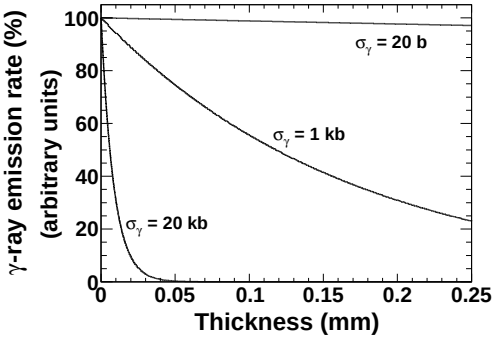

Figure 10: Probability for γ-ray emission as a function of the depth in the capture sample illustrated for different capture cross sections.

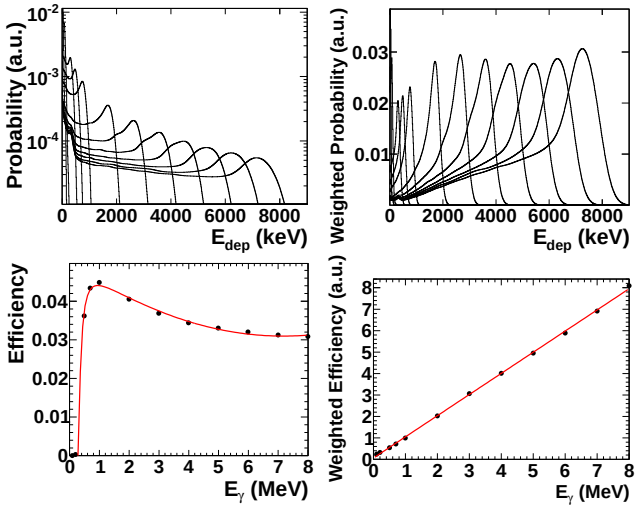

Figure 11: (Color online) Simulated response functions before (top-left) and after weighting (top-right). By the weighting procedure the original energy dependence of the efficiency (bottom-left) becomes proportional to the energy of the registered γ-rays (bottom-right).

dependence of the spatial profile of the n_TOF neutron beam [23] has no effect on the calculated WFs.

The γ-ray emission probability across the sample thickness shows a strong dependence on the cross section as illustrated in Fig. 10 (at the example of three fictitious (n,γ) cross sections). While a large cross section leads to a surface-peaked γ-ray emission profile, small cross section resonances show a rather flat γ-ray emission. Depending on the sample-detector geometry this effect may give rise to large γ-ray absorption corrections.

In previous measurements it was found that this effect requires the use of a particular WF, which can be obtained by means of a linear regularization method [47, 54]. An alternative approach consists in using negative-degree polynomials [42]. When the absorption of low energy capture γ-rays is large, both methods lead to a monotonically decreasing WF below $E_\gamma \approx 200$ keV. In view of this difficulty a rather thin gold sample of 1.5×10^{-3} at/b was chosen in the present measurements, where the absorption effect for low energy γ-rays is sufficiently small that the conventional use of polynomial WFs remains valid within $\geq$99.4% as it is demonstrated below in Sec. IV B 2. The parameters of these polynomial WFs are obtained following the common least squares approach,

$$min \sum_j (\sum_i W_i R_i^j - \alpha E_{\gamma j})^2 \qquad (8)$$

where R_i^j is the MC simulated response function for γ-ray events of a certain initial energy $E_{\gamma j}$. An example of MC simulated responses for γ-ray energies between 100 keV and 8 MeV is shown in the top-left panel of Fig. 11. The weighting function W_i was approximated by a 4-degree polynomial,

$$W_i = \sum_{k=0}^{4} a_i E_i^k. \qquad (9)$$

After weighting of the response functions (Fig. 11 top-right) the efficiency becomes proportional ($\alpha = 1$) to γ-ray energy (Fig. 11 bottom) as it is required by the PHWT. The unweighted γ-ray efficiency of the system is shown for comparison in the bottom-left panel of Fig. 11.

2. *Uncertainty of the WF*

The accuracy of the calculated WFs is estimated by simulating a capture experiment, where the compound nucleus ^{198}Au de-excites by a γ-ray cascade [25, 54]. Because the systematic uncertainty in the determination of the capture yield is of pivotal relevance for the present work, this approach is briefly summarized. Let us assume $\mathcal{R}^c$ to be the response function of the C_6D_6 detection system for N capture events with a fixed capture energy E_c and let $\mathcal{W}$ be the calculated weighted function. The PHWT requires that

$$\mathcal{W} \cdot \mathcal{R}^c = N E_c, \qquad (10)$$

where $\mathcal{W} \cdot \mathcal{R}^c$ designates the weighted sum of the response function of the detection system,

$$\mathcal{W} \cdot \mathcal{R}^c = \sum W_i R_i^c. \qquad (11)$$

This sum includes the entire energy range from 0 up to the maximum energy deposited by the capture γ-rays.

From Eq. 10 one can define an *accuracy estimator* which equals 1 in the ideal case.

$$f_R = \frac{\mathcal{W} \cdot \mathcal{R}^c}{N E_c}. \qquad (12)$$

Deviations from $f_R = 1$ can be interpreted as an estimate of the uncertainty of the applied WF itself, i. e., on

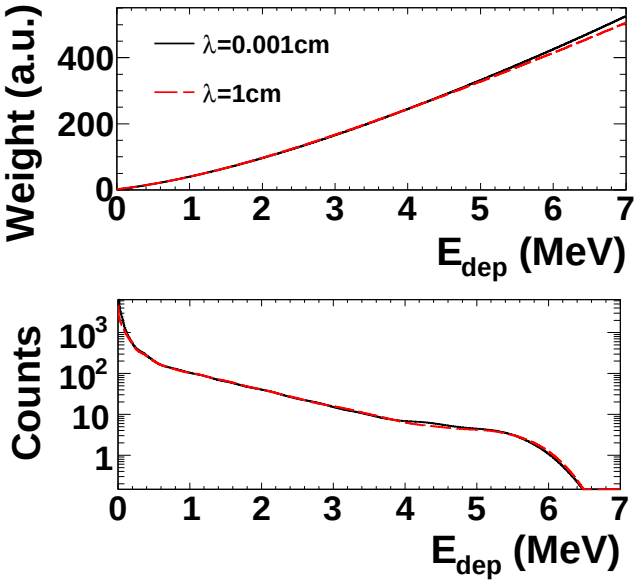

Figure 12: (Color online) Top: Four degree polynomial WFs obtained for two different neutron absorption rates. Bottom: Response function of the C_6D_6 detector system for simulated γ-ray cascades from the 4.9 eV resonance in Au. The specific neutron absorption coefficient $\lambda = A/\rho N_A \sigma_\gamma$ is determined by the radiative capture cross section σ_γ in cm^2 and the sample density ρ in (g/cm^3). A and N_A denote atomic number and Avogadro number.

$\mathcal{W}$. In this calculation, the decay γ-rays of the compound nucleus were simulated using the computer code DECAYGEN [58], which has been extensively used and validated both in β-decay experiments with high efficiency NaI(Tl) detectors [59] as well as for γ-ray cascades following neutron captures measured with the n_TOF TAC [60] and with C_6D_6 detectors [54]. The simulated response function $\mathcal{R}^c$ of the C_6D_6 detector system for the 4.9 eV resonance in ^{197}Au is shown in the bottom panel of Fig. 12. The WFs for the extreme cases of a surface peaked neutron absorption (4.9 eV resonance) and of a flat neutron capture profile (4.8 keV resonance) are plotted in the upper panel of Fig. 12.

Following the approach described above, ratios between $f_R = 0.9936$ and $f_R = 0.9993$ were found, confirming that the polynomial WFs calculated for the present gold sample introduce an uncertainty of 0.6% in the determination of the capture yield.

C. Experimental effects and corrections

There are several experimental effects, which need to be properly taken into account in order to keep the systematic uncertainty in the yield determination at the 2% level [25].

These effects are summarized by the factor $f_{\rm exp}$ in Eq. 7 and refer to

- γ-ray summing,
- conversion electrons,
- low energy threshold,
- γ-ray depth profile.

As described in Refs. [47, 54, 57, 61], these effects can be quantified by means of MC simulations of the complete capture γ-ray cascades. The correction for γ-ray summing, when two γ-rays from the same cascade are recorded by the detector, can be estimated from the difference between the response function if the γ-rays in the prompt capture cascade are simulated sequentially (no summing) and simultaneously (summing).

Conversion electrons are taken into account via the event generator DECAYGEN by including fluorescence yields and electron binding energies (K-, L- and M-shells) in the MC simulation of the de-excitation cascade in ^{198}Au. The pulse-height threshold of ≈200 keV in the C_6D_6 spectra implies the response function to be zero below 200 keV. Due to the Compton nature of the C_6D_6 pulse height spectra, this effect has the largest impact on the measured capture yield. It can be estimated as

$$f_{\rm thr} = \frac{\mathcal{W} \cdot \mathcal{R}^c}{\mathcal{W} \cdot \mathcal{R}^{c,t}}. \qquad (13)$$

In this expression $\mathcal{R}^{c,t}$ is the simulated response function truncated at 200 keV.

The resulting corrections for the measured capture yield are summarized in Table III.

Table III: Corrections of the capture yield due to experimental effects.

Effect	Correction (%)
γ-ray summing	1.7(5)
Conversion electrons	-0.4(5)
γ-ray threshold (200 keV)	5.5(6)
γ-ray absorption	< 0.5

The yield scaling factor

$$f_{exp} = \frac{N E_c}{\sum_{200\ keV} W_i R_i^c} = 1.067(3), \qquad (14)$$

was determined by simulating all effects together and comparing the resulting response function with the ideal case. In total $N = 5 \times 10^5$ capture events have been simulated in both cases.

D. Background

Apart from the effects discussed so far, there are two remaining sources of background at the measuring station. The component between thermal and ∼200 eV (see Fig. 13) arises from neutrons scattered in the sample,

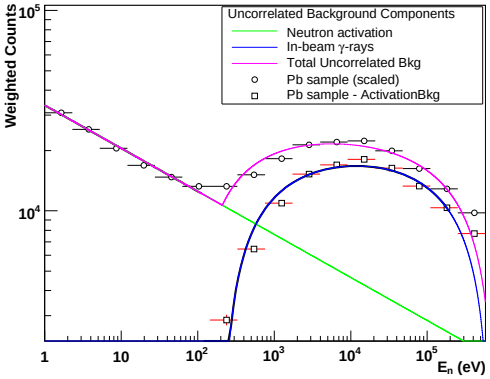

Figure 13: (Color online) Energy dependence of the background components at n_TOF determined from the measurement of a lead sample. At lower neutron energies, the ambient background due to thermal neutron activation shows the expected exponential trend. At higher neutron energies the background is dominated by delayed in-beam γ-rays (see text for details).

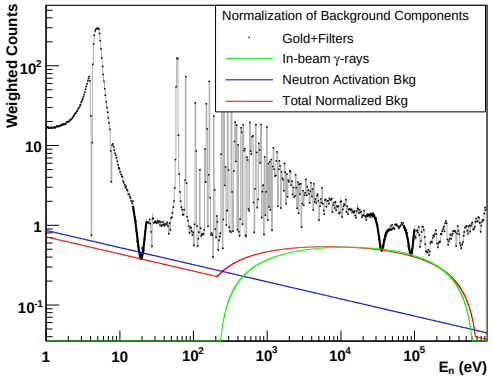

Figure 14: (Color online) Capture yield of Au with Al and W filters in the beam to determine the background level.

which are thermalized and captured somewhere in the experimental area. This ambient background level is rather small. Contributions from neutrons which do not interact with the sample are practically negligible, thus the neutron beam-line continues about 12 m beyond the capture experiment to the beam-dump, which is separated from the experimental area by a thick concrete wall.

The second type of background contributes significantly in the energy range between 200 eV and ~500 keV (see Fig. 13) and it is due to delayed in-beam γ-rays from neutron captures in the water moderator of the spallation source. In fact, these γ-rays can be scattered by the sample. The origin and the energy dependence of both background components was determined from a dedicated measurement with a lead sample as shown in Fig. 13.

The relative contribution from each background component to the measurement of the gold sample was obtained in a series of measurements with the gold sample in combination with neutron filters of Al and W. The filters, which are installed at a flight path of 135 m, were thick enough that the strongest resonances became black, thus showing the effective background level at these neutron energies. The effect of the black resonances on the Au capture yield was fitted as a smooth perturbation of the reaction yield as illustrated in Fig. 14.

V. RESULTS

A. From capture yield to cross section

The self-shielding corrected capture yield

$$Y_{\rm th} = (1 - e^{-n\sigma_{tot}})\frac{\sigma_\gamma}{\sigma_{tot}} \qquad (15)$$

is related to the capture cross section σ_γ and to the total cross section σ_{tot} where n is the areal density of the sample.

The net capture yields in the RRR obtained from the TAC and C_6D_6 data can be expressed in terms of the resonance parameters,

$$Y_\gamma(E_n) = Y_\gamma(E_n, \vec{a}), \qquad (16)$$

where the vector of resonance parameters

$$\vec{a} = (J_{\rm i}^\pi, \ell, E_{\rm R,i}, \Gamma_{\gamma,{\rm i}}, \Gamma_{\rm n,i}) \quad \text{with i=1, m} \qquad (17)$$

includes the m = 268 resonances contained in both data sets in the energy range between 1 eV and 5 keV.

These capture yields were analyzed using the R-matrix analysis code SAMMY [18]. The yield is parameterised via the Multi-Level Breit Wigner (MLBW) formalism using a scattering radius of 9.658 fm [17] and a temperature of 293 K for the correction of the Doppler effect. Other experimental effects, i. e. multiple neutron scattering in the sample and neutron self-shielding are properly taken into account within the SAMMY code. Although for the majority of the resonances the width is dominated by the Doppler broadening, the resonance broadening due to the n_TOF resolution function is also considered in the SAMMY fits by the implemented RPI-parameterization [18]. The parameters for this function were determined in a series of measurements on narrow resonances at higher neutron energies [24].

The fitting procedure allowed us to extract the resonance parameters from the measured capture yields, although in many cases only the resonance energy $E_{\rm R}$ and the total capture kernel $g\Gamma_\gamma\Gamma_n/\Gamma$ should be considered as the real measurable quantities. Only in cases where one of the channels dominates over the other, $\Gamma_n >> \Gamma_\gamma$ or $\Gamma_n << \Gamma_\gamma$, the resonance shape analysis is sufficiently sensitive to the smaller value. Otherwise, the resonance parameters are given in square brackets in Table IV to indicate that they have to be taken with some caution. The quoted resonance energies are the ones measured with the C_6D_6 detectors.

Resonance parameters from the ENDF/B-VII data [16] library were used as initial values in our fits. In general, we tried to vary as few parameters as possible (either Γ_n or Γ_γ), but when the improvement in the χ^2 value of the fit was substantial, both parameters (Γ_n and Γ_γ) were allowed to vary.

Because both analyses were performed independently, the comparison of the resulting data sets provides an estimate of the overall systematic uncertainty and reveals the benefits and drawbacks of both capture detectors. However, a common R-matrix analysis of both data sets is beyond the scope of the present work. In any case, a complete re-evaluation of the cross section and its potential recognition as a capture standard requires also the combined analysis of data sets, including transmission data, of other facilities. In this context, the present results provide relevant information on the capture kernels and in some cases on the resonance parameters.

Examples of the fitted yield are shown in Fig. 15 and Fig. 16, where the data points stand respectively for the C_6D_6 and TAC measurement, the dotted curve represents the evaluated data listed in ENDF/B-VII database [16], and the solid curve the actual MLBW fits to the present data.

The resonance parameters and the radiative kernels derived from the C_6D_6 and TAC data are listed in Tab. IV. Parameters without uncertainties have been kept fixed in the analysis. Otherwise, the standard deviation of the fitted parameter is quoted as the corresponding uncertainty.

Table IV: Resonance parameters[1,2,3] extracted from the R-matrix analysis of the n_TOF C_6D_6 and TAC data.

			C_6D_6			TAC		
E_R (eV)	J	ℓ	Γ_n (meV)	Γ_γ (meV)	$g\Gamma_n\Gamma_\gamma/\Gamma$ (meV)	Γ_n (meV)	Γ_γ (meV)	$g\Gamma_n\Gamma_\gamma/\Gamma$ (meV)
4.905	2	0	15.2	124	8.5	15.2	124	8.5
(36.07)[a]								
46.63	1	0	0.223 ± 0.006	128	0.084 ± 0.002	0.220 ± 0.008	128	0.082 ± 0.003
58.02	1	0	4.34 ± 0.05	112	1.57 ± 0.02	4.43 ± 0.05	112	1.60 ± 0.02
60.23	2	0	[73.93 ± 0.29]	110	27.63 ± 0.12	[72.7 ± 0.4]	110	27.36 ± 0.09
78.44	1	0	17.79 ± 0.18	120	5.81 ± 0.06	16.6 ± 0.2	120	5.48 ± 0.05
107.0	2	0	8.29 ± 0.10	110	4.82 ± 0.06	7.9 ± 0.1	110	4.63 ± 0.05
122.2	2	0	0.86 ± 0.02	128	0.53 ± 0.01	0.89 ± 0.03	128	0.55 ± 0.02
144.3	1	0	9.35 ± 0.15	120	3.25 ± 0.05	8.8 ± 0.2	120	3.08 ± 0.05
151.3	2	0	[21.6 ± 0.4]	[149.7 ± 5.1]	11.8 ± 0.6	[22.7 ± 0.4]	[141 ± 5]	12.2 ± 0.2
162.9	1	0	[42.5 ± 1.1]	[196.8 ± 8.0]	13.1 ± 0.8	[46 ± 1]	[170 ± 7]	13.6 ± 0.3
165.0	2	0	8.67 ± 0.14	109	5.02 ± 0.08	9.1 ± 0.2	109	5.24 ± 0.09
189.9	1	0	[49.8 ± 0.9]	130	13.5 ± 0.2	[48.13 ± 0.9]	130	13.2 ± 0.2
209.0[b]	1	0	[0.86 ± 0.04]	[181.9 ± 28.1]	0.32 ± 0.07	[0.87 ± 0.09]	[190 ± 60]	0.32 ± 0.03
240.4	2	0	[86.6 ± 2.1]	[99.6 ± 1.9]	29.0 ± 1.0	[82 ± 7]	[98 ± 7]	27.9 ± 1.6
255.4[b]	1	0	[0.50 ± 0.05]	[129.2 ± 39.7]	0.19 ± 0.08	[0.58 ± 0.09]	[120 ± 60]	0.22 ± 0.03
262.1	1	0	[151.7 ± 3.7]	[124.0 ± 2.4]	25.6 ± 0.9	[167 ± 8]	[108 ± 3]	24.6 ± 0.6
273.7	2	0	4.41 ± 0.12	110	2.65 ± 0.07	5.0 ± 0.2	110	3.0 ± 0.1
293.2	2	0	[347.7 ± 4.6]	[123.6 ± 1.5]	57.0 ± 1.2	[336 ± 7]	[128 ± 2]	57.9 ± 0.7
329.2	2	0	[41.5 ± 1.0]	137	19.9 ± 0.5	[42 ± 1]	137	20.2 ± 0.4
330.6	1	0	[56.2 ± 1.8]	130	14.7 ± 0.5	[59 ± 2]	130	15.3 ± 0.4
355.3	2	0	37.6 ± 0.9	125	18.1 ± 0.4	37.8 ± 1.0	125	18.13 ± 0.4
370.9	2	0	[108.9 ± 3.6]	99	32.4 ± 1.2	[101 ± 4]	99	31.3 ± 0.6
375.4	1	0	12.32 ± 0.42	125	4.21 ± 0.14	12.5 ± 0.6	125	4.3 ± 0.2
381.8	2	0	[73.9 ± 2.4]	97	26.2 ± 0.9	[70 ± 2]	97	25.5 ± 0.5
400.1	2	0	6.08 ± 0.23	128	3.63 ± 0.14	6.4 ± 0.4	128	3.8 ± 0.2
401.3	1	0	25.8 ± 0.8	140	8.2 ± 0.3	25 ± 1	140	7.9 ± 0.3
440.1	1	0	281.4	[149.3 ± 3.0]	36.6 ± 0.8	281.4	[129 ± 3]	33.1 ± 0.6
450.8	2	0	[63.7 ± 2.0]	110	25.2 ± 0.8	[67 ± 2]	110	26.0 ± 0.6
477.1	2	0	296.1	[124.9 ± 2.2]	54.9 ± 1.0	296.1	[118 ± 3]	52.8 ± 0.8
489.5	1	0	[62.2 ± 2.1]	138	16.1 ± 0.6	[57 ± 2]	138	15.1 ± 0.4
493.6	2	0	28.5 ± 0.8	111	14.2 ± 0.4	26.4 ± 1.0	111	13.3 ± 0.4
533.6	2	0	31.8 ± 1.0	130	16.0 ± 0.5	32.5 ± 0.5	130	16.2 ± 0.2
548.1	1	0	[58.6 ± 2.2]	127	15.0 ± 0.6	[61 ± 1]	127	15.4 ± 0.2
561.2	2	0	2.44 ± 0.19	128	1.49 ± 0.12	2.5 ± 0.1	128	1.52 ± 0.07
578.5	2	0	288.4	[126.0 ± 3.1]	54.8 ± 1.4	288.4	[132 ± 2]	56.7 ± 0.5
580.4	1	0	306.8	[121.7 ± 4.0]	32.7 ± 1.1	306.8	[103 ± 2]	28.9 ± 0.4
586.3	2	0	22.4 ± 0.8	134	12.0 ± 0.4	22.4 ± 0.4	134	12.0 ± 0.2
602.4	2	0	223.9	[112.6 ± 2.6]	46.8 ± 1.1	223.9	[113 ± 1]	47.0 ± 0.4
616.9	1	0	[111.1 ± 5.2]	135	22.9 ± 1.2	[117 ± 3]	135	23.5 ± 0.3

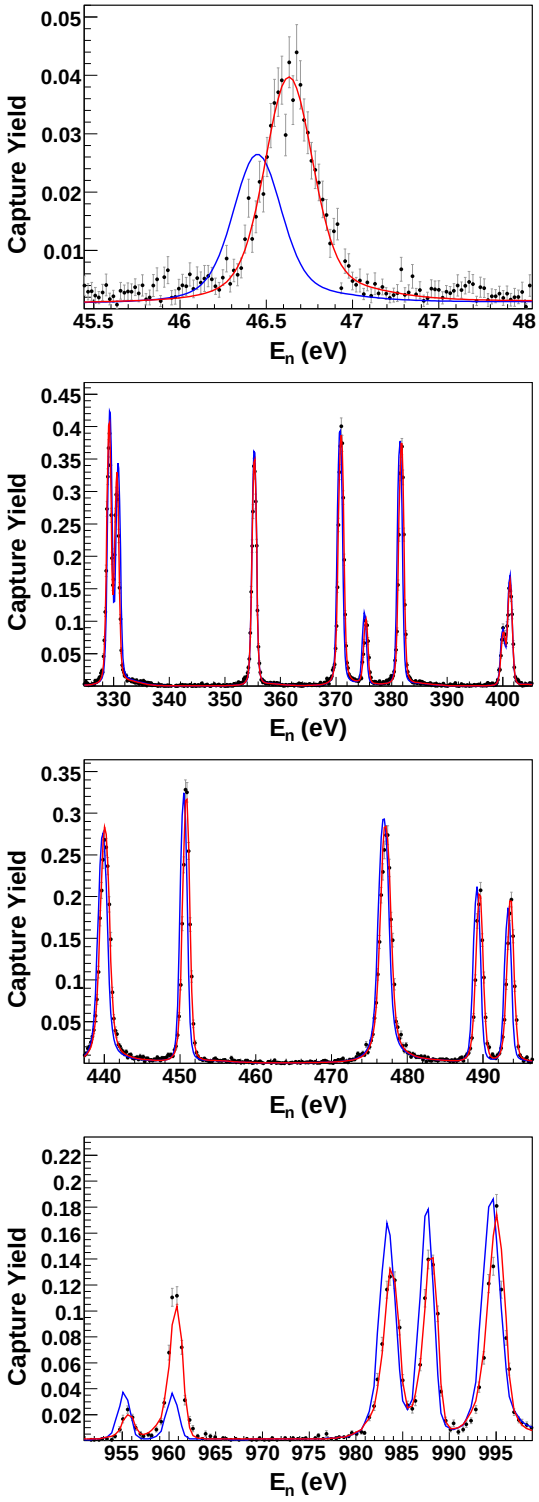

Figure 15: (Color online) Examples for resonance fits of the C_6D_6 data (solid symbols with error bars). The blue dotted represents the evaluated data listed in ENDF/B-VII database [16] and the solid curve shows the present fits.

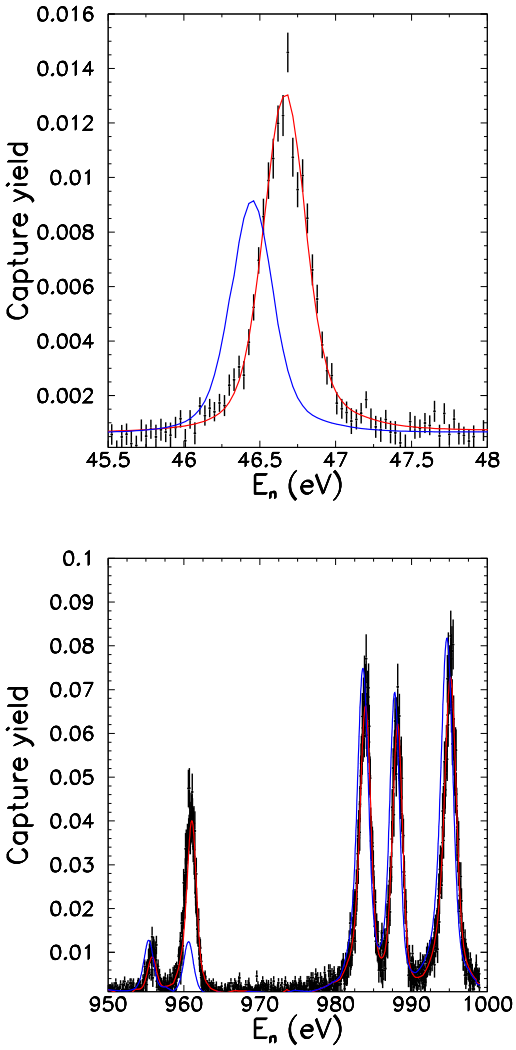

Figure 16: (Color online) Examples for resonance fits of the TAC data (solid symbols with error bars). The blue dotted represents the evaluated data listed in ENDF/B-VII database [16] and the solid curve shows the present fits.

624.1	1 0 [53.4 ± 2.3]	121	13.9 ± 0.6	[53 ± 1]	121	13.9 ± 0.2
627.9	2 0 24.7 ± 0.8	138	13.1 ± 0.5	25.3 ± 0.4	138	13.4 ± 0.2
638.3	2 0 464.0	[118.5 ± 2.5]	59.0 ± 1.3	464.0	[118 ± 1]	58.9 ± 0.5
658.4	2 0 4.21 ± 0.30	97	2.52 ± 0.18	4.7 ± 0.2	97	2.8 ± 0.1
685.6	1 0 16.8 ± 0.9	128	5.6 ± 0.3	18.7 ± 0.5	128	6.12 ± 0.15
695.3	1 0 666.7	138.5 ± 4.0	43.0 ± 1.3	666.7	128 ± 2	40.3 ± 0.5
698.5	2 0 736.1	109.8 ± 3.2	59.7 ± 1.8	736.1	115 ± 1	62.2 ± 0.6
715.2	2 0 [111.0 ± 20.2]	[112.0 ± 18.0]	34.8 ± 9.4	[105.7 ± 10.0]	[120 ± 5]	35 ± 2
738.0	1 0 10.6 ± 0.7	120	3.7 ± 0.2	11.3 ± 0.4	120	3.9 ± 0.14
759.5	1 0 426.7	[110.3 ± 3.2]	32.9 ± 1.0	426.7	116 ± 2	34.2 ± 0.4
773.3	1 0 474.6	[125.0 ± 3.8]	37.1 ± 1.1	474.6	[127 ± 2]	37.6 ± 0.4
783.8	2 0 [14.0 ± 4.9]	140	37.3 ± 1.9	[102 ± 2]	140	36.8 ± 0.4
795.5	2 0 177.6	[122.7 ± 4.2]	45.4 ± 1.7	177.6	[124 ± 2]	45.7 ± 0.4
812.8	1 0 22.1 ± 1.3	128	7.1 ± 0.4	23.4 ± 0.7	128	7.4 ± 0.2
819.0	2 0 [231.6 ± 21.9]	[127.6 ± 4.6]	51.4 ± 6.1	[245 ± 15]	[121 ± 3]	50.6 ± 1.3
824.4	2 0 426.4	[116.6 ± 3.3]	57.2 ± 1.7	426.4	[121 ± 2]	59.0 ± 0.6
863.7	2 0 18.4	106.7 ± 26.0	9.8 ± 3.1	18.4	160 ± 20	10.3 ± 0.2

878.9	2	0	35.2	[65.5 ± 6.7]	14.3 ± 1.7	35.20	[59 ± 3]	13.8 ± 0.3
931.8	2	0	[339.9 ± 25.0]	[123.5 ± 3.7]	56.6 ± 5.5	[350 ± 20]	[127 ± 2]	58 ± 1
955.4	2	0	6.3 ± 0.5	128	3.7 ± 0.3	5.8 ± 0.3	128	3.4 ± 0.2
960.6	2	0	[49.2 ± 2.2]	150	23.1 ± 1.1	[56 ± 1]	150	25.6 ± 0.4
983.6	2	0	[244.5 ± 35.9]	[93.8 ± 3.5]	42.4 ± 7.9	[300 ± 20]	[106 ± 2]	49 ± 1
987.8	2	0	[94.4 ± 4.9]	160	37.1 ± 2.0	[95 ± 3]	160	[37.3 ± 0.6]
994.8	2	0	[348.3 ± 30.1]	130	59.2 ± 6.3	[410 ± 20]	130	61.9 ± 0.6
1039.1	1	0	[44.6 ± 3.0]	128	12.4 ± 0.9	[41 ± 2]	128	11.7 ± 0.4
1042.6	1	0	485.4	[107.8 ± 4.1]	33.1 ± 1.3	485.4	[119 ± 2]	35.8 ± 0.6
1063.2	1	0	9.5 ± 0.9	128	3.3 ± 0.3	11.1 ± 0.6	128	3.8 ± 0.2
1077.3	1	0	360.0	[119.1 ± 4.8]	33.6 ± 1.4	360.0	[121 ± 3]	34.0 ± 0.6
1092.0	2	0	375.9	[98.3 ± 3.5]	48.7 ± 1.8	375.91	[99 ± 2]	48.9 ± 0.7
1119.6	2	0	11.7 ± 0.9	128	6.7 ± 0.5	11.1 ± 0.5	128	6.4 ± 0.3
1127.9	2	0	28.8 ± 1.7	128	14.7 ± 0.9	28.1 ± 1.0	128	14.4 ± 0.4
1134.8	2	0	[349.9 ± 30.3]	[127.0 ± 4.5]	58.2 ± 6.6	[290 ± 20]	[136 ± 4]	58 ± 2
1177.1	2	0	6.6 ± 0.6	128	3.9 ± 0.4	6.6 ± 0.4	128	3.9 ± 0.2
1182.7	2	0	289.6	[107.4 ± 4.0]	[49.0 ± 1.9]	289.6	[124 ± 3]	54.35 ± 0.8
1206.6	2	0	360.0	[108.9 ± 4.4]	52.3 ± 2.2	360.0	[110 ± 2]	52.93 ± 0.8
1217.8	2	0	24.5 ± 1.6	128	12.9 ± 0.8	23.5 ± 1.0	128	12.4 ± 0.4
1222.7	1	0	[502.1 ± 57.8]	120	36.3 ± 5.4	[560 ± 30]	120	37.1 ± 0.4
1244.6	1	0	[155.9 ± 13.5]	128	26.4 ± 2.6	[220 ± 10]	128	30.4 ± 0.6
1252.6	2	0	38.4 ± 2.2	128	18.5 ± 1.1	42 ± 1	128	19.7 ± 0.5
1281.1	1	0	458.8	115.7 ± 5.2	34.6 ± 1.6	458.8	117 ± 3	35.1 ± 0.7
1285.5	2	0	13.0 ± 1.1	128	7.4 ± 0.6	15.7 ± 0.7	128	8.7 ± 0.4
1309.9	2	0	252.8	[100.0 ± 4.3]	44.8 ± 2.0	252.8	[105 ± 3]	46.5 ± 0.8
1327.9	1	0	704.0	124.7 ± 5.4	39.7 ± 1.7	704.0	122± 3	39.2 ± 0.8
1335.2	2	0	[80.7 ± 4.9]	131	31.2 ± 2.0	[94 ± 3]	131	34.1 ± 0.7
1353.5	1	0	592.1	[200.8 ± 8.6]	56.2 ± 2.5	592.1	[192 ± 5]	54.4 ± 1.0
1358.9	2	0	18.6 ± 1.4	128	10.2 ± 0.8	21.0 ± 0.9	128	11.3 ± 0.4
1366.9	2	0	[147.9 ± 46.3]	[102.0 ± 15.1]	37.7 ± 15.0	[160 ± 10]	[111 ± 7]	41 ± 2
1394.9	2	0	32.1 ± 2.0	128	16.0 ± 1.0	33.6 ± 1.3	128	16.6 ± 0.5
1425.8	1	0	261.3	[124.9 ± 11.1]	31.7 ± 3.0	261.3	[123 ± 7]	31 ± 1
1428.1	2	0	424.7	102.3 ± 5.7	51.5 ± 2.9	424.7	108 ± 3	54 ± 1
1449.5	2	0	[296.4 ± 39.9]	97	45.7 ± 7.7	[310.0 ± 20.9]	97	46.2 ± 0.7
1468.8	2	0	27.5 ± 2.0	128	14.1 ± 1.0	30.3 ± 1.3	128	15.3 ± 0.5
1473.8	1	0	[160.0 ± 18.5]	128	26.7 ± 3.5	[143.5 ± 8.1]	128	25.4 ± 0.7
1489.5	2	0	820.1 ± 62.2	134	72.0 ± 7.2	1035.0	159 ± 3	86 ± 2
1500.8	1	0	28.4 ± 3.1	128	8.7 ± 1.0	27.4 ± 1.6	128	8.5 ± 0.4
1529.5	1	0	[48.2 ± 4.4]	128	13.1 ± 1.2	[42 ± 2]	128	11.9 ± 0.5
1551.4	2	0	[104.8 ± 8.0]	135	36.9 ± 3.1	[120 ± 5]	135	39.7 ± 0.9
1568.4	2	0	5.3 ± 0.8	128	3.2 ± 0.5	5.5 ± 0.4	128	3.3 ± 0.3
1577.8	1	0	480.1	112.2 ± 6.1	34.1 ± 1.9	480.1	137 ± 4	39.9 ± 0.9
1592.4	2	0	[38.3 ± 3.0]	128	18.4 ± 1.5	[40 ± 2]	128	19.1 ± 0.6
1614.1	2	0	[131.9 ± 12.9]	120	39.3 ± 4.4	[150 ± 8]	120	41.7 ± 1.0
1634.0[b]	1	0	8.1 ± 4.1	118.9 ± 59.4	2.8 ± 2.4	7.7 ± 0.7	119 ± 12	2.7 ± 0.2
1640.8	1	0	[106.0 ± 11.7]	128	21.7 ± 2.6	[121 ± 7]	128	23.3 ± 0.7
1645.4	2	0	[89.4 ± 6.9]	128	32.9 ± 2.7	[99 ± 4]	128	34.9 ± 0.9
1658.7	1	0	4.3 ± 2.1	128	1.6 ± 0.8	4.3 ± 0.4	128	1.5 ± 0.1
1692.4	2	0	[101.7 ± 7.9]	148	37.7 ± 3.2	[110 ± 5]	148	39.3 ± 1.0
1705.3	2	0	270.4	[105.7 ± 5.8]	47.5 ± 2.7	270.4	[127 ± 4]	53.9 ± 1.2
1720.5	2	0	25.7 ± 2.3	128	13.4 ± 1.2	29 ± 2	128	14.7 ± 0.6
1733.5	2	0	315.2	[94.3 ± 5.1]	45.4 ± 2.5	315.2	[106 ± 3]	49.4 ± 1.2
1753.5	2	0	320.0	[121.2 ± 8.8]	54.9 ± 4.1	320	[123 ± 6]	56 ± 2
1755.6	1	0	567.9	108.5 ± 11.1	34.2 ± 3.6	567.9	125 ± 7	38 ± 2
1810.8	1	0	[72.9 ± 7.7]	128	17.4 ± 2.0	[85.5 ± 4.9]	128	19.2 ± 0.7
1820.7	2	0	13.8 ± 1.6	128	7.8 ± 0.9	13.6 ± 0.9	128	7.7 ± 0.5
1830.9	1	0	[66.1 ± 7.2]	128	16.4 ± 1.9	[74 ± 5]	128	17.6 ± 0.7
1855.6	1	0	1386.4	128.2 ± 7.6	44.0 ± 2.6	1386.4	130 ± 5	44.4 ± 1.4
1859.6	2	0	[73.5 ± 7.3]	128	29.2 ± 3.1	[89 ± 5]	128	32.8 ± 1.0
1882.6	1	0	[108.3 ± 11.5]	156	24.0 ± 2.7	[144 ± 8]	156	28.1 ± 0.8
1892.2	2	0	2.9 ± 1.4	128	1.8 ± 0.9	2.9 ± 0.3	128	1.8 ± 0.2
1912.7	1	0	2450.2	117.1 ± 7.0	41.9 ± 2.5	2450.2	119 ± 4	42.6 ± 1.4
1939.0	1	0	[412.0 ± 89.7]	128	36.6 ± 10.0	[360 ± 30]	128	35.4 ± 0.8

1959.5	2	0	874.5 ± 99.3	128	69.8 ± 10.5	1160 ± 70	128	72.1 ± 0.4
2021.1	1	0	18.6 ± 2.9	128	6.1 ± 0.9	14 ± 2	128	4.7 ± 0.6
2028.0	1	0	[438.6 ± 132.1]	128	37.2 ± 14.1	[370 ± 60]	128	35.7 ± 1.4
2032.3	1	0	426.0	101.1 ± 9.7	30.6 ± 3.0	426.0	118 ± 8	35 ± 2
2035.3	2	0	[156.5 ± 21.9]	128	44.0 ± 7.0	[165 ± 15]	128	45 ± 2
2058.6	2	0	19.3 ± 2.4	128	10.5 ± 1.3	17.6 ± 1.5	128	9.7 ± 0.7
2074.9	2	0	1080.2	97.9 ± 5.7	56.1 ± 3.3	1080.2	98 ± 3	56 ± 2
2081.7	2	0	[574.7 ± 121.9]	128	65.4 ± 17.9	[242 ± 20]	128	52 ± 2
2088.4	1	0	[254.3 ± 53.2]	128	31.9 ± 8.0	[250 ± 30]	128	31.7 ± 1.2
2111.7	2	0	[59.3 ± 5.6]	128	25.3 ± 2.5	[64 ± 4]	128	26.6 ± 1.1
2130.7	1	0	1327.1 ± 201.7	128	43.8 ± 9.0	980 ± 130	128	42.4 ± 0.7
2147.4	2	0	491.2	107.0 ± 6.3	54.9 ± 3.3	491.2	106 ± 4	54.5 ± 1.6
2153.8	1	0	[152.7 ± 22.4]	128	26.1 ± 4.4	[183 ± 18]	128	28.2 ± 1.1
2192.9	1	0	[324.4 ± 54.6]	128	34.4 ± 7.1	[318 ± 37]	128	34.2 ± 1.1
2223.3	1	0	[51.5 ± 7.2]	128	13.8 ± 2.0	[50 ± 4]	128	13.5 ± 0.8
2240.4	2	0	[86.5 ± 9.0]	128	32.3 ± 3.6	[69 ± 5]	128	28.1 ± 1.3
2278.1	2	0	15.7 ± 2.2	128	8.8 ± 1.3	14.2 ± 1.3	128	8.0 ± 0.7
2286.4[d]	2	0	(190.6 ± 24.4)	128	(47.9 ± 7.1)	(150 ± 10)	128	(43.0 ± 1.4)
2331.9	2	0	[202.4 ± 26.8]	128	49.0 ± 7.6	[210 ± 20]	128	49.7 ± 1.6
2366.1	2	0	[399.6 ± 85.9]	128	60.6 ± 16.3	[250 ± 25]	128	53 ± 2
2379.6	2	0	3.8 ± 1.2	128	2.3 ± 0.7	3.8 ± 0.8	128	2.3 ± 0.4
2405.8	2	0	[100.3 ± 11.6]	128	35.1 ± 4.5	[91 ± 7]	128	33.3 ± 1.5
2414.5	1	0	1066.3	164.3 ± 12.0	53.4 ± 3.9	1066.3	170 ± 8	55 ± 2
2419.1	2	0	1119.8	48.0 ± 5.2	28.8 ± 3.1	1119.8	52 ± 3	31.2 ± 1.8
2440.0	1	0	[115.6 ± 19.2]	128	22.8 ± 4.2	[131.0 ± 12.7]	128	24.3 ± 1.2
2469.1	2	0	528.1	98.6 ± 6.8	51.9 ± 3.6	528.1	98 ± 4	52 ± 2
2498.1	2	0	37.0 ± 4.5	128	18.0 ± 2.2	35.8 ± 3	128	17.5 ± 1.2
2507.7	2	0	[49.4 ± 5.9]	128	22.3 ± 2.8	[50.1 ± 4.0]	128	22.5 ± 1.3
2535.1	2	0	[83.5 ± 10.1]	128	31.6 ± 4.1	[74.4 ± 5.6]	128	29.4 ± 1.4
2560.1	2	0	16.7 ± 2.7	128	9.2 ± 1.5	16.2 ± 3.3	128	9.0 ± 1.6
2576.8	1	0	[202.5 ± 40.3]	128	29.4 ± 6.9	[210 ± 30]	128	29.7 ± 1.6
2581.3	2	0	10.9 ± 2.2	128	6.3 ± 1.3	10.3 ± 1.9	128	6.0 ± 1.0
2597.6	2	0	256.0	[100.8 ± 8.4]	45.2 ± 3.9	256	[106 ± 6]	46.8 ± 1.8
2611.6	2	0	272.0	[95.1 ± 7.8]	44.0 ± 3.7	272	[100 ± 5]	45.6 ± 1.7
2628.0	2	0	17.2 ± 2.7	128	9.5 ± 1.5	17.1 ± 3.4	128	9.4 ± 1.7
2632.3	1	0	8.0 ± 2.4	128	2.8 ± 0.9	8.0 ± 1.6	128	2.8 ± 0.5
2652.6[c]	1	0						
2683.8	2	0	[70.4 ± 8.3]	124	28.1 ± 3.5	[73 ± 6]	124	28.7 ± 1.5
2708.2	1	0	[207.6 ± 74.4]	[217.3 ± 77.4]	39.8 ± 22.5	[210 ± 30]	[222 ± 33]	40.7 ± 4.2
2722.4	2	0	[151.0 ± 23.6]	124	42.6 ± 7.6	[161 ± 15]	124	44 ± 2
2747.2	2	0	[86.0 ± 11.2]	124	31.7 ± 4.5	[99 ± 8.5]	124	34.4 ± 1.6
2761.5	2	0	[88.8 ± 11.5]	124	32.4 ± 4.5	[95.7 ± 8.2]	124	33.8 ± 1.6
2774.8	1	0	11.8 ± 3.2	124	4.0 ± 1.1	11.1 ± 2.0	124	3.8 ± 0.6
2790.5	1	0	20.8 ± 4.8	124	6.7 ± 1.6	20.5 ± 4.1	124	6.6 ± 1.1
2805.4	2	0	154.1 ± 22.8	124	42.9 ± 7.3	168 ± 17	124	44.6 ± 1.9
2831.7	2	0	303.0	67.9 ± 6.6	34.7 ± 3.4	303.0	57 ± 4	30.1 ± 1.7
2849.5	2	0	[55.5 ± 7.0]	124	24.0 ± 3.2	[67.6 ± 5.7]	124	27.3 ± 1.5
2864.3	2	0	[122.3 ± 16.7]	124	38.5 ± 5.9	[158 ± 15]	124	43.5 ± 1.8
2876.0	2	0	[123.8 ± 19.2]	124	38.7 ± 6.7	[107.4 ± 9.8]	124	36.0 ± 1.8
2896.1[c]	1	0						
2910.8	1	0	8.8 ± 2.7	124	3.1 ± 0.9	9.2 ± 1.8	124	3.2 ± 0.6
2926.8	2	0	2.9 ± 1.1	124	1.8 ± 0.7	2.9 ± 0.6	124	1.8 ± 0.3
2957.1	1	0	[47.6 ± 8.6]	124	12.9 ± 2.4	[51.0 ± 6.4]	124	13.5 ± 1.2
2985.1	2	0	214.0	[83.6 ± 9.1]	37.6 ± 4.2	214	[83 ± 6]	37.3 ± 1.9
3023.9	2	0	[488.5 ± 148.8]	124	61.8 ± 24.1	470	[113 ± 10]	56.7 ± 3.9
3036.6	2	0	991.9 ± 199.8	124	68.9 ± 18.6	730	126 ± 9	67.1 ± 4.1
3048.4	1	0	[185.9 ± 42.4]	124	27.9 ± 7.4	303	[110 ± 16]	30.3 ± 3.3
3063.0	2	0	3.6 ± 1.3	124	2.2 ± 0.8	4.6 ± 3.2	124	2.8 ± 1.9
3079.0	1	0	[133.9 ± 27.1]	124	24.1 ± 5.5	502.0	[87 ± 12]	27.7 ± 3.2
3098.3	1	0	[44.7 ± 8.5]	124	12.3 ± 2.4	[43.5 ± 10.1]	124	12.1 ± 2.1
3133.5	2	0	[220.6 ± 44.0]	124	49.6 ± 11.7	216.0	[97 ± 12]	41.9 ± 3.4
3160.9	1	0	14.9 ± 4.3	124	5.0 ± 1.5	17.9 ± 7.9	124	5.9 ± 2.3
3174.2	1	0	[59.3 ± 11.4]	124	15.0 ± 3.0	[82.0 ± 24.4]	124	18.5 ± 3.3

3200.2	1	0	10.4 ± 3.5	124	3.6 ± 1.2	8.7 ± 7.3	124	3.0 ± 2.4
3214.8[d]	2	0	(1519.7 ± 259.4)	144	(82.2 ± 19.0)	330	(109 ± 10)	(51.1 ± 3.7)
3254.0	2	0	[84.1 ± 14.1]	124	31.3 ± 5.7	[102.9 ± 18.0]	124	35.2 ± 3.4
3258.3	1	0	[139.2 ± 35.3]	124	24.6 ± 7.1	[145.9 ± 46.0]	124	25.1 ± 3.6
3268.7	2	0	[48.9 ± 7.8]	124	21.9 ± 3.6	[51.4 ± 11.1]	124	22.7 ± 3.5
3278.2	2	0	[76.1 ± 11.4]	124	29.5 ± 4.7	[80.3 ± 15.6]	124	30.5 ± 3.6
3302.3[c]	1	0						
3310.0[c]	2	0						
3333.4	2	0	[253.9 ± 58.1]	124	52.1 ± 14.4	650	101 ± 12	54.6 ± 5.8
3347.4	2	0	531.9 ± 142.9	140	69.3 ± 23.7	980	153 ± 11	82.8 ± 5.0
3362.8	2	0	[127.8 ± 21.4]	124	39.3 ± 7.4	200	[105 ± 16]	43.1 ± 4.2
3385.1	2	0	[246.7 ± 61.7]	124	51.6 ± 15.5	270	[105 ± 15]	47.2 ± 4.8
3399.8	2	0	543.2 ± 120.3	131	66.0 ± 18.8	702	149 ± 14	76.7 ± 6.1
3416.6	1	0	5.4 ± 2.4	124	2.0 ± 0.9	3.41 ± 3.35	124	1.25 ± 1.19
3439.1	1	0	19.4 ± 5.1	124	6.3 ± 1.7	22.6 ± 13.1	124	7.15 ± 3.5
3469.6	2	0	460.0	80.5 ± 7.9	42.8 ± 4.3	460	102 ± 12	52.1 ± 5.0
3489.3	1	0	[77.6 ± 16.4]	124	17.9 ± 4.1	[76 ± 25]	124	17.7 ± 3.6
3511.9	2	0	[134.7 ± 24.1]	124	40.4 ± 8.1	[113 ± 23]	124	36.9 ± 4.0
3518.9	1	0	[98.4 ± 22.0]	124	20.6 ± 5.0	[89.4 ± 30.6]	124	19.5 ± 3.9
3540.3	2	0	[89.2 ± 16.2]	124	32.4 ± 6.4	[83.3 ± 18.3]	124	31.1 ± 4.1
3548.7	2	0	980.0	141.6 ± 11.8	77.3 ± 6.5	980	126 ± 14	69.6 ± 6.8
3565.6	2	0	236.0	[63.8 ± 8.2]	31.4 ± 4.1	236	[86 ± 13]	39.3 ± 4.3
3593.9	2	0	416.4 ± 86.7	210	87.2 ± 21.8	1650	178 ± 12	100.5 ± 6.0
3637.7	2	0	[166.5 ± 32.7]	124	44.4 ± 10.0	450	[97 ± 12]	49.9 ± 5.2
3652.1	2	0	2.9 ± 1.3	124	1.8 ± 0.8	6.0 ± 3.2	124	3.6 ± 1.8
3671.1	1	0	[60.6 ± 13.4]	124	15.3 ± 3.5	[68.6 ± 27.6]	124	16.6 ± 4.3
3690.4	2	0	[47.8 ± 8.6]	124	21.6 ± 4.0	[73 ± 18]	124	28.6 ± 4.4
3695.7	1	0	35.4 ± 8.6	124	10.3 ± 2.6	14.6 ± 7.4	124	4.9 ± 2.2
3708.5	1	0	[55.2 ± 12.3]	124	14.3 ± 3.3	[47.3 ± 21.2]	124	12.8 ± 4.2
3727.6	2	0	[272.8 ± 73.9]	124	53.3 ± 17.5	413	[95 ± 13]	48.1 ± 5.5
3743.9	1	0	28.5 ± 7.2	124	8.7 ± 2.2	24 ± 15	124	7.6 ± 4.0
3759.7	1	0	24.6 ± 8.3	124	7.7 ± 2.6	(40.3 ± 15.8)	124	(11.4 ± 3.4)
3762.4	2	0	17.7 ± 5.1	124	9.7 ± 2.8	(13.0 ± 8.1)	124	(7.4 ± 4.1)
3789.4	1	0	3.3 ± 1.6	124	1.2 ± 0.6	4.1 ± 3.5	124	1.5 ± 1.2
3807.0	2	0	[128.9 ± 24.0]	124	39.5 ± 8.3	217	[74 ± 14]	34.6 ± 4.9
3841.3	2	0	[213.6 ± 50.2]	124	49.0 ± 13.6	525	114 ± 12	58.3 ± 5.1
3863.1	1	0	19.2 ± 6.1	124	6.2 ± 2.0	31.7 ± 16.6	124	9.5 ± 3.9
3871.6	2	0	[197.2 ± 47.1]	124	47.6 ± 13.3	384	[100 ± 17]	49.6 ± 6.7
3887.7	2	0	[341.1 ± 96.1]	124	56.8 ± 19.9	600	104 ± 13	55.2 ± 6.1
3913.9	2	0	859.5 ± 261.3	144	77.1 ± 30.9	925	154 ± 15	82.4 ± 6.7
3939.8	2	0	1104.5 ± 309.0	153	84.0 ± 31.3	1092	154 ± 15	84.6 ± 7.2
3964.4	2	0	[136.9 ± 27.6]	124	40.7 ± 9.3	268	[76 ± 16]	37.2 ± 6.0
3981.9	2	0	3771.5 ± 568.2	148	89.0 ± 18.6	1270	87 ± 13	50.7 ± 6.9
3986.9	1	0	[42.1 ± 14.9]	124	11.8 ± 4.3	[57.7 ± 24.6]	124	14.8 ± 4.3
3999.3	2	0	[52.5 ± 10.4]	124	23.1 ± 4.8	[31.7 ± 27.7]	124	15.8 ± 11.0
4036.6	2	0	740.5 ± 261.9	123	65.9 ± 30.7	918.0	110 ± 18	61.5 ± 8.9
4046.7[c]	1	0						
4072.9	1	0	43.4 ± 12.1	124	12.1 ± 3.5	23.9 ± 12.5	124	7.5 ± 3.3
4085.9	2	0	859.2 ± 302.8	141	75.7 ± 35.2	997	150 ± 17	81.5 ± 7.8
4126.8	2	0	2158.5 ± 465.1	165	95.8 ± 28.2	846	174 ± 16	90.3 ± 6.8
4137.3	1	0	[46.1 ± 11.9]	124	12.6 ± 3.4	291	[60 ± 22]	18.7 ± 5.6
4164.1	2	0	[87.1 ± 17.8]	124	32.0 ± 7.1	[77.7 ± 22.1]	124	29.8 ± 5.2
4170.9	2	0	[170.8 ± 74.1]	[87.5 ± 24.8]	36.1 ± 21.7	[74.8 ± 23.9]	124	29.2 ± 5.8
4232.9	2	0	30.8 ± 6.8	124	15.4 ± 3.5	42.1 ± 13.6	124	19.7 ± 4.7
4248.1	2	0	391.1 ± 126.8	124	58.8 ± 23.9	465	78 ± 12	41.9 ± 5.4
4273.4	1	0	[41.4 ± 11.3]	124	11.6 ± 3.3	[61.5 ± 24.8]	124	15.4 ± 4.2
4288.9	2	0	[85.3 ± 17.4]	124	31.6 ± 6.9	[54.1 ± 19.0]	124	23.5 ± 5.8
4300.6	2	0	460.3 ± 178.1	124	61.1 ± 30.1	470	85 ± 16	45.1 ± 7.0
4315.4[d]	2	0	(2887.4 ± 577.8)	124	(74.3 ± 20.6)	350	(82 ± 18)	(41.4 ± 7.4)
4332.3	2	0	[114.5 ± 25.3]	124	37.2 ± 9.1	[160.7 ± 46.8]	124	43.8 ± 5.5
4355.6	1	0	163.5 ± 82.9	22.6 ± 8.1	7.4 ± 5.7	176.5 ± 93.6	79 ± 33	20.4 ± 6.7
4364.4	2	0	[129.4 ± 27.5]	124	39.6 ± 9.4	[94.7 ± 34.2]	124	33.6 ± 6.9
4388.6	1	0	297.0 ± 91.4	124	32.8 ± 12.4	334	66 ± 24	20.6 ± 6.4

4422.2	2	0	455.0	85.6 ± 11.2	45.0 ± 6.0	455	118 ± 21	58.4 ± 8.1
4435.8	2	0	34.6 ± 7.5	124	16.9 ± 3.8	[93.1 ± 35.4]	122 ± 53	33.0 ± 9.5
4455.2	1	0	[60.6 ± 15.6]	124	15.3 ± 4.1	[69.8 ± 31.1]	124	16.7 ± 4.8
4521.2	2	0	[219.1 ± 59.3]	124	49.5 ± 15.9	440	[103 ± 16]	52.1 ± 6.6
4535.7	1	0	[423.1 ± 183.2]	124	36.0 ± 19.7	415	[121 ± 29]	35.1 ± 6.5
4541.7	2	0	[80.6 ± 18.6]	124	30.5 ± 7.6	[81.8 ± 28.4]	124	30.8 ± 6.4
4551.8	1	0	[52.0 ± 14.8]	124	13.7 ± 4.1	[91.9 ± 30.0]	124	19.8 ± 3.7
4572.6	2	0	652.6 ± 263.8	124	65.1 ± 34.4	484	75 ± 19	40.8 ± 9.0
4589.8	2	0	[50.8 ± 11.4]	124	22.5 ± 5.3	[67.3 ± 22.4]	124	27.3 ± 5.9
4610.9	1	0	23.7 ± 7.8	124	7.5 ± 2.5	37 ± 20.3	124	10.7 ± 4.5
4626.6	2	0	2.2 ± 1.2	124	1.4 ± 0.7	5.1 ± 3.1	124	3.0 ± 1.8
4665.6	2	0	1551.0 ± 467.9	138	79.2 ± 32.4	970	94 ± 16	53.5 ± 8.3
4684.0	2	0	[166.3 ± 42.2]	124	44.4 ± 13.0	[148.2 ± 49.4]	124	42.2 ± 6.4
4695.9	1	0	[90.1 ± 26.3]	124	19.6 ± 6.2	[60.9 ± 29.4]	124	15.3 ± 5.0
4713.5	1	0	[191.6 ± 60.3]	124	28.2 ± 10.4	[116.9 ± 55.0]	124	22.6 ± 5.5
4732.4	2	0	[78.2 ± 18.9]	124	30.0 ± 7.8	[55.4 ± 18.8]	124	23.9 ± 5.6
4766.2	2	0	[43.9 ± 9.8]	124	20.3 ± 4.7	[68.4 ± 27.1]	124	27.6 ± 7.0
4780.4	2	0	[186.2 ± 50.3]	124	46.5 ± 14.7	283	[69 ± 22]	34.8 ± 8.9
4789.3	2	0	[157.1 ± 40.5]	124	43.3 ± 12.8	[122.6 ± 44.1]	124	38.5 ± 7.0
4800.8	1	0	[60.0 ± 17.9]	124	15.2 ± 4.8	[38.7 ± 17.6]	124	11.1 ± 3.8
4828.8	2	0	[262.4 ± 123.2]	[78.6 ± 16.4]	[37.8 ± 23.8]	[247 ± 128]	88 ± 22	40.7 ± 9.3
(4869.1)[a]								(36 ± 8)[e]
(4880.4)[a]								(42 ± 7)[e]
(4892.2)[a]								(69 ± 19)[e]
(4915.7)[a]								(67 ± 20)[e]
(4944.0)[a]								(65 ± 18)[e]
(5000.4)[a]								(41 ± 12)[e]
(5012.2)[a]								(31 ± 6)[e]

[1] Quantum numbers, J^π and ℓ, taken form ENDF/B-VII.
[2] Parameters in square brackets have to be taken with caution (see text).
[3] Parameters in parentheses indicate cases with large systematic uncertainties.
[a] First determination in a capture experiment.
[b] Not included in ENDF/B-VII.
[c] Probably not a resonance.
[d] Probably doublet.
[e] Average value from TAC and C_6D_6.

B. Discussion of uncertainties

The total uncertainties in the capture yields measured with the TAC and the C_6D_6 detectors are summarized in Table V. Apart from the contribution by the energy dependence of the neutron flux, the total uncertainties of the two methods are dominated by completely independent components. In both cases, the largest uncertainty of 3% is caused by the energy dependence of the neutron flux.

A more specific discussion of the TAC related uncertainties shows that a 2% uncertainty is caused by the fact that the sample was smaller than the diameter of the neutron beam. The difference between the related normalization factors extracted from parasitic and dedicated data is about 0.5%. From this difference and from the uncertainty of the dead-time correction in the 4.9 eV resonance an uncertainty of 1% was estimated for the normalization by the saturated resonance technique. The dead-time correction as such was only significant for the stronger resonances. The background determined by the measurement without sample was normalized by means of the number of protons per pulse, which carries an uncertainty of 1%. The uncertainty due to the neutron sensitivity of the TAC is taken into account in the resonance shape analysis.

The situation for the C_6D_6 data differs in several respects. In this case the 2% uncertainty of the PHWT contributed strongly to the overall uncertainty. While the uncertainty of the background subtraction was similar to the TAC analysis, the normalization procedure was not affected by dead-time effects, which were negligible for the smaller C_6D_6 detectors. Moreover the influence of the detector thresholds is small because the γ-ray spectra for the different resonances are quite similar because of the large number of levels available for decay after neutron capture. Therefore, the normalization of the C_6D_6 data is affected by an uncertainty of only 0.5%.

The sum of these components yields an overall systematic uncertainty of 3.5% for the C_6D_6 and 3.9-4.1% (depending on the count rate) for the TAC results, as listed in Table V.

Table V: Different components of estimated systematic or correlated uncertainty in the measured capture yields.

Component	Uncertainty (%)	
	C_6D_6	TAC
PHWT	2	-
Normalization	0.5	1
Dead time	-	0 - 1.2
Background	1	1
Flux shape	3	3
Beam profile [62]	< 0.5	2
Total	3.5 - 3.8	3.9 - 4.1

C. Comparison between TAC and C_6D_6 results

The capture kernel $g\Gamma_n\Gamma_\gamma/\Gamma$ is a quantity proportional to the area of a resonance, which is sensitive to systematic effects related to the measurement technique. Therefore, the ratio of the capture kernels obtained from the TAC and C_6D_6 data is discussed with respect to several quantities and their respective systematic uncertainties.

The ratio in Fig. 17 shows good agreement between the TAC and C_6D_6 results with an average deviation of less than 2%, thus confirming that the absolute normalization of the capture yield in both independent analyses was consistent and reliable. As shown in the bottom panel of Fig. 17, the RMS deviation between both data sets is less than 8% as expected due to different experimental effects in the two data sets as well as to the uncertainty introduced by the resonance shape analysis.

The absence of a correlation between the kernels and their ratios provides evidence for the accuracy of WF as illustrated in Fig. 18 and indicates that the γ-ray attenuation in the sample was properly treated in the C_6D_6 data. The figure shows also that larger deviations are related to weak resonances. The overall good agreement indicates also that the individual resonance-related corrections applied in the analysis of the TAC data, namely neutron sensitivity and dead-time corrections, are consistent with the C_6D_6 results, where these corrections have practically no impact.

Fig. 19 illustrates that the kernel ratio as a function of TAC count rate is fully consistent for the strong resonances (and high counting rates). Only for small resonances there are discrepancies between the two data sets, similar to the case of Fig. 18.

The proper treatment of the neutron sensitivity correction in the TAC data is supported by the absence of a clear trend between the kernel ratios and the Γ_n/Γ_γ ratios shown in Fig. 20. This main correction for the TAC data is further confirmed by the plot of the kernel ratio versus resonance strength $g\Gamma_n$ in Fig. 21.

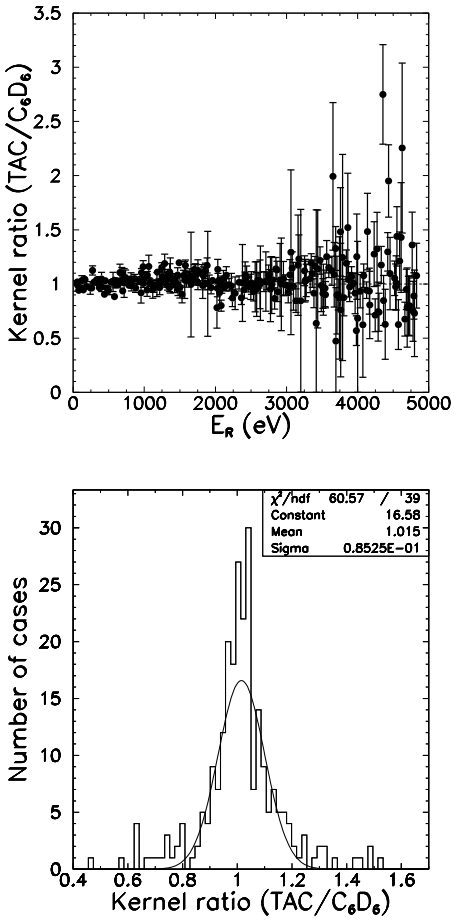

Figure 17: (Color online) Top: Ratio of capture kernels versus resonance energy. Bottom: The statistical distributions of the kernel ratios agree within 1.5% at an average standard deviation of about 8.5%.

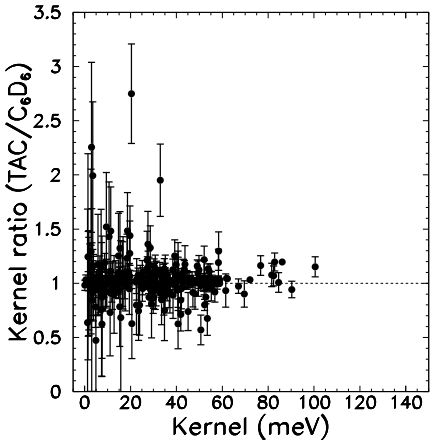

Figure 18: Comparison of the capture kernels obtained from the TAC data and C_6D_6 data as a function of resonance area.

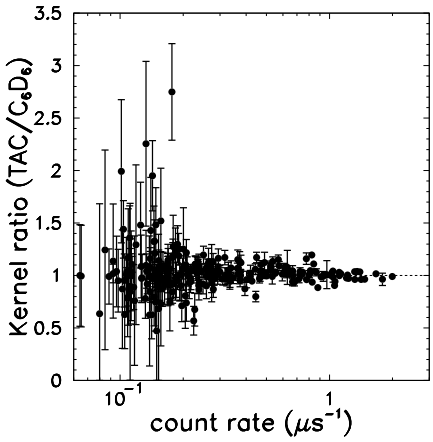

Figure 19: Comparison of the capture kernels obtained from the TAC and C_6D_6 data as a function of peak resonance count rate of TAC data.

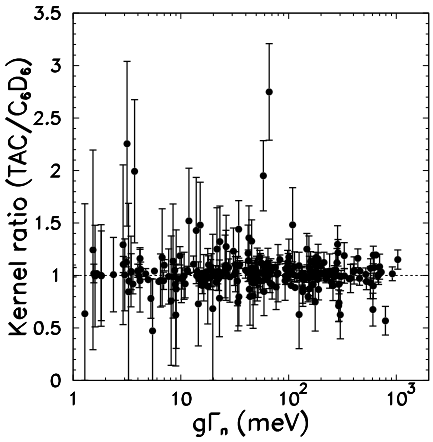

Figure 21: Comparison of the capture kernels obtained from the TAC and C_6D_6 data as a function of the resonance strength $g\Gamma_n$.

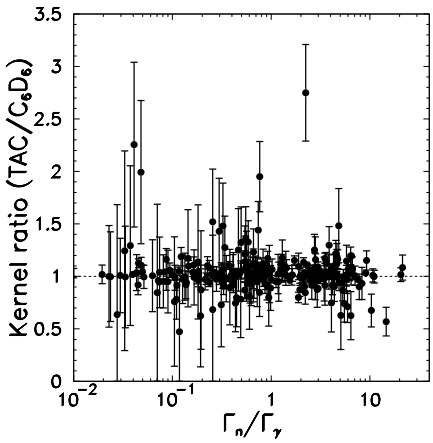

Figure 20: Comparison of the capture kernels obtained from the TAC and C_6D_6 data versus Γ_n/Γ_γ.

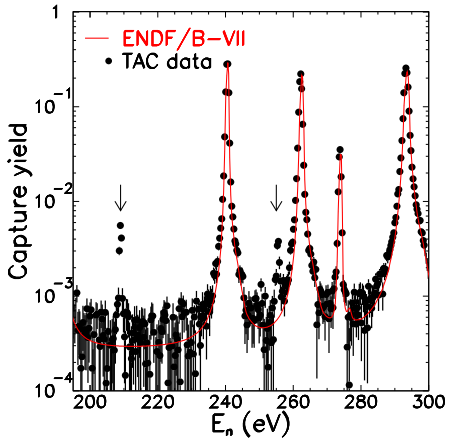

Figure 22: (Color online) Capture yield reconstructed from the ENDF/B-VII parameters and the corresponding TAC data. The resonances at 209 and 255 eV are not included in the evaluation.

D. Comparison with libraries

With respect to the ENDF/B-VII evaluation we observed:

- three resonances not included in the evaluation, at 209, 255, and 1634 eV (Fig. 22);
- six new resonances at 4869.1, 4880.4, 4892.2, 4915.7, 4944.0, and 5000.4 eV in the energy range above previous analyses (Fig. 23);
- a structure at 36.07 eV, that is probably a resonance;
- resonances at 2286.4, 3214.8, and 4315.4 eV, which are probably doublets;
- features at 2652.6, 2896.1, 3302.3, 3310.0, and 4046.7 eV, which are probably due to multiple scattering in nearby resonances rather than genuine resonances as quoted in ENDF/B-VII (Fig. 24).

On average, the present capture kernels are 10-15% lower than the values from ENDF/B-VII. There is a systematic trend for the discrepancies to increase with neutron energy as shown for the C_6D_6 and the TAC data in the top panels of Figs. 25 and 26, respectively.

VI. CONCLUSIONS

The ^{197}Au(n,γ) reaction has been measured at n_TOF with the aim of improving the accuracy of the neutron capture cross section in the resolved resonance region. To identify and to minimize systematic uncertainties, espe-

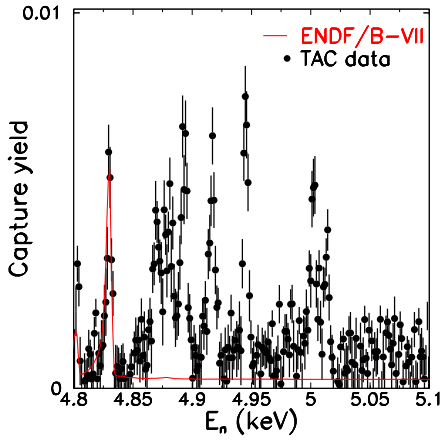

Figure 23: (Color online) Capture yield reconstructed from the ENDF/B-VII parameters and the corresponding TAC data. The evaluation ends at 4.83 keV.

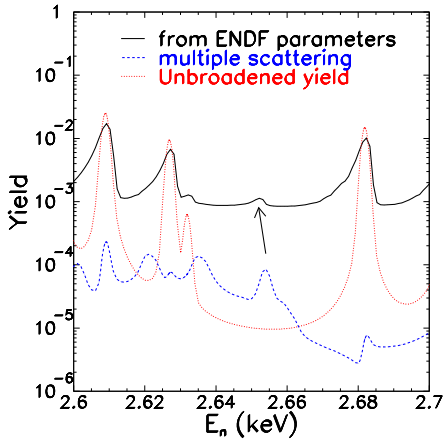

Figure 24: (Color online) Capture yield calculated from the ENDF/B-VII parameters and folded with the experimental resolution (thick solid line) compared to the contribution from multiple scattering, which was calculated without the resonance at 2652.6 (dotted line). The structure indicated by the arrow is probably due to multiple scattering.

cially those related to the detection efficiency and to the neutron sensitivity, two conceptually different detection systems have been employed, a total absorption calorimeter (TAC), and a total energy system based on hydrogen-free C_6D_6 liquid scintillators. The conditions used in the analysis of the TAC data were suitably chosen to reduce backgrounds as far as possible, notably the effect of neutron scattering from the sample. Corrections were applied to account for the dead-time and the neutron sensitivity of the TAC data. For the C_6D_6 measurement the accurate weighting function technique was used, which was developed for the n_TOF setup. The data were then corrected for threshold effects and for electron conversion of the capture γ-rays in the sample.

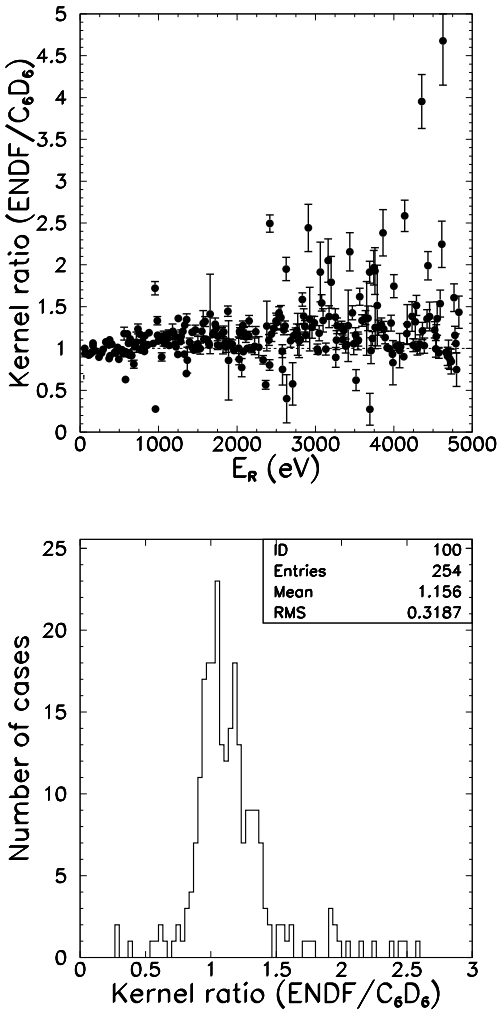

Figure 25: Top: Ratio of capture kernels from ENDF/B-VII and the present C_6D_6 results vs. resonance energy. Bottom: The corresponding distribution of the ratios.

The resonances measured with the two different systems were separately analyzed with the code SAMMY in order to extract the radiative kernels. A total of 268 resonances, from 1 eV to about 5 keV were analyzed. The comparison of the results obtained with the two detectors showed very good agreement with an average systematic difference of only 2%, thus confirming the high accuracy of the data. An 8% RMS deviation between the capture kernels extracted from the two data sets indicates that an uncertainty of less than 5% per detector has been reached for most of the resonances. Some larger differences may partially be attributed to residual effects related to the neutron sensitivity of the TAC or to the background subtraction for the smallest resonances. Six new resonances have been identified in the energy region between 4.83 keV and 5 keV. Three resonances that had been removed in the ENDF/B-VII evaluation compared to the ENDF/B-VI version have been clearly observed. On the

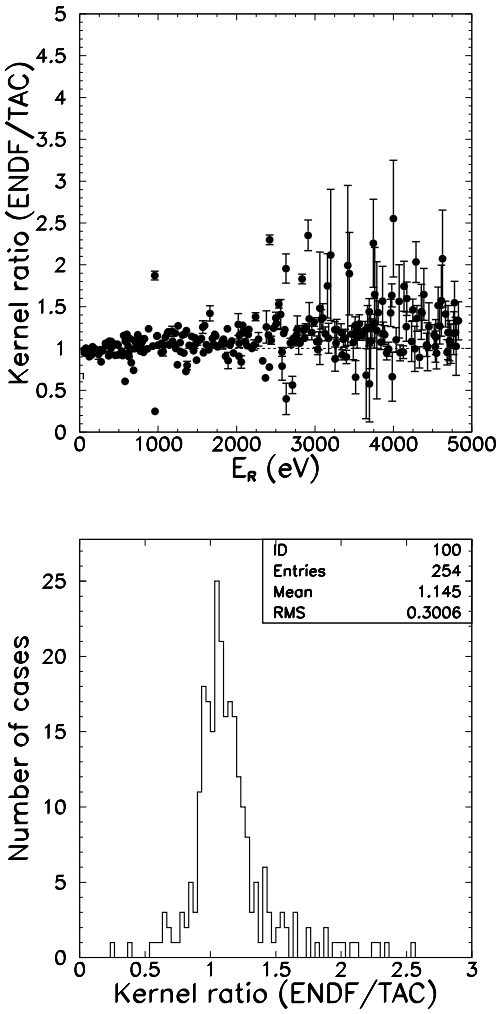

Figure 26: Top: Ratio of capture kernels from ENDF/B-VII and the present TAC results vs. resonance energy. Bottom: The corresponding distribution of the ratios.

contrary, five resonances listed in the evaluations seem to be caused by multiple scattering background from nearby resonances.

A combination of the two data sets will allow to obtain results with an estimated uncertainty close to 4% for the capture resonances. In combination with high-accuracy transmission data, the present results may be used to extract very accurate resonance parameters, eventually leading to the extension of the Au cross section as a capture standard in the resolved resonance region.

[1] G. Wallerstein *et al.*, Rev. Mod. Phys **69**, 955 (1997).

[2] F. Käppeler, Progress in Particle and Nuclear Physics **43**, 419 (1999), ISSN 0146–6410.

[3] W. Gudowski, Nuclear Physics A **752**, 623 (2005), ISSN 0375–9474.

[4] NEA-OEDC Report (2002), ISBN 92-64-18482-1.

[5] M. Salvatores and I. Slessarev and V. Berthou, Progress in Nuclear Energy **38**, 167 (2001), ISSN 0149–1970.

[6] *International Evaluation of Neutron Cross Section Standards* (2007), International Atomic Energy Agency, STI/PUB/1291.

[7] L. R. Macklin, J. Halperin, and R. R. Winters, Nucl. Instrum. Methods **164**, 213 (1979), ISSN 0029-554X.

[8] J. S. Desjardins, J. L. Rosen, W. W. Havens, and J. Rainwater, Phys. Rev. **120**, 2214 (1960).

[9] M. Asghar, M. C. Moxon and C. M. Chaffey, in *Proceedings of the International Conference on the study of Nuclear Structure with Neutrons*, edited by M. Néve de Mévergines, P. Van Assche and J. Verneir (North-Holland Publishing Co., Amsterdam, 1965), p. 522.

[10] J. Julien, S. D. Barros, G. Bianchi, C. Corge, V. D. Huynh, G. L. Poittevin, J. Morgenstern, F. Netter, C. Samour, and R. Vastel, Nuclear Physics **76**, 391 (1966), ISSN 0029-5582.

[11] J. Lynn and E. Rae, Journal of Nuclear Energy **4**, 418 (1957), ISSN 0891-3919.

[12] R. N. Alves, J. Julien, J. Morgenstern, and C. Samour, Nuclear Physics A **131**, 450 (1969), ISSN 0375-9474.

[13] R. L. Macklin, J. Halperin, and R. R. Winters, Phys. Rev. C **11**, 1270 (1975).

[14] M. M. Hoffman, W. M. Sanders, G. J. Berzins, L. J. Brown, and D. D. Phillips, *Neutron scattering cross section of* ^{197}Au (1974), LANL Report, LA-5552.

[15] P. G. Young (1984), LANL, USA, ENDF/B-VI evalua-

tion, MAT # 7925, revision 1, July 1991, data retrieved from the ENDF database.
[16] P. G. Young (1984), LANL, USA, ENDF/B-VI evaluation, MAT # 7925, revision 2, Dec 2006, data retrieved from the ENDF database.
[17] S. F. Mughabghab, *Neutron Cross Sections: Neutron Resonance Parameters and Thermal Cross Sections* (Academic press, New York, 2006).
[18] N. M. Larson, "Updated users' guide for SAMMY: Multilevel R-matrix fits to neutron data using Bayes' equations", SAMMY computer code, Report ORNL/TM-9179/R7, Oak Ridge National Laboratory.
[19] C. Lederer *et al.*, Phys. Rev. C, in preparation.
[20] S. Abramovich *et al.*, Tech. Rep. CERN-SPSC-99-8. SPSC-P-310, CERN, Geneva (1999).
[21] U. Abbondanno *et al.*, Technical Report CERN-SL-2002-053 ECT (2003).
[22] F. Gunsing *et al. (The n_TOF Collaboration)*, Nucl. Instrum. Methods B **261**, 925 (2007), ISSN 0168-583X.
[23] J. Pancin *et al. (The n_TOF Collaboation)*, Nucl. Instrum. Methods A **524**, 102 (2004).
[24] G. Lorusso *et al. (The n_TOF Collaboration)*, Nucl. Instrum. Methods A **532**, 622 (2004).
[25] U. Abbondanno *et al. (The n_TOF Collaboration)*, Nucl. Instrum. Methods A **521**, 454 (2004).
[26] URL http://www.acqiris.com.
[27] R. Plag, M. Heil, F. Käppeler, P. Pavlopoulos, R. Reifarth, and K. Wisshak, Nucl. Instrum. Methods A **496**, 425 (2003).
[28] K. H. Guber, L. C. Leal, R. O. Sayer, P. E. Koehler, T. E. Valentine, H. Derrien, and J. A. Harvey, Nucl. Instrum. Methods B **241**, 218 (2005).
[29] K. H. Guber, L. C. Leal, R. O. Sayer, P. E. Koehler, T. E. Valentine, H. Derrien, and J. A. Harvey, in *International Conference on Nuclear Data for Science and Technology, Santa Fe, New Mexico, 2004* (2005), vol. 769 of *American Institute of Physics Conference Series*, pp. 1706–1711.
[30] R. L. Macklin and J. H. Gibbons, Phys. Rev. **159**, 1007 (1967).
[31] C. Guerrero *et al. (The n_TOF Collaboration)*, Nucl. Instrum. Methods A **608**, 424 (2009), ISSN 0168-9002.
[32] E. Berthoumieux *et al. (The n_TOF Collaboration)*, in *Proceedings of the International Conference on Nuclear Data for Science and Technology, Nice, France, 2007*, edited by O. Bersillon *et al., EDP Sciences* (CEA, Paris, 2008, 2007), p. 627.
[33] C. Massimi *et al. (The n_TOF Collaboration)* , in *Proceedings of the International Conference on Nuclear Data for Science and Technology, Nice, France, 2007* , edited by O. Bersillon *et al., EDP Sciences* (CEA, Paris, 2008, 2007), p. 1265.
[34] C. Lampoudis *et al. (The n_TOF Collaboration)*, in *Proceedings of the International Conference on Nuclear Data for Science and Technology, Nice, France, 2007*, edited by O. Bersillon *et al., EDP Sciences* (CEA, Paris, 2008, 2007), p. 595.
[35] D. Cano-Ott *et al. (The n_TOF Collaboration)*, in *Proceedings of the International Conference on Nuclear Data for Science and Technology, Nice, France, 2007*, edited by O. Bersillon *et al., EDP Sciences* (CEA, Paris, 2008, 2007), p. 627.
[36] S. Marrone *et al. (The n_TOF Collaboration)*, Nucl. Instrum. Methods A **517**, 389 (2004).
[37] C. Borcea *et al.*, Nucl. Instrum. Methods A **513**, 524 (2003).
[38] S. Marrone *et al.*, Nucl. Instrum. Methods A **568**, 904 (2006), ISSN 0168 - 9002.
[39] G. F. Knoll, *Radiation Detection and Measurement* (J. Wiley & Sons, 1989).
[40] K. Wisshak, K. Guber, F. Käppeler, J. Krisch, H. Müller, G. Rupp and F. Voss, Nucl. Instrum. Methods A **292**, 595 (1990), ISSN 0168-9002.
[41] F. Corvi, in *Proceedings Specialists Meeting on Measurement, Calculation and Evaluation of Photon production data*, edited by C. Coceva *et al.* (1994), pp. 229–246, report NEA/NSC/DOC(95)1.
[42] A. Borella, G. Aerts, F. Gunsing, M. Moxon, P. Schillebeeckx, and R. Wynants, Nucl. Instrum. Methods A **577**, 626 (2007).
[43] M. Heil, R. Reifarth, M. M. Fowler, R. C. Haight, F. Käppeler, R. S. Rundberg, E. H. Seabury, J. L. Ullmann, J. B. Wilhelmy, and K. Wisshak, Nucl. Instrum. Methods A **459**, 229 (2001), ISSN 0168-9002.
[44] R. Reifarth, T. A. Bredeweg, A. Alpizar-Vicente, J. C. Browne, E. I. Esch, U. Greife, R. C. Haight, R. Hatarik, A. Kronenberg, J. M. O'Donnell, et al., Nucl. Instrum. Methods A **531**, 530 (2004), ISSN 0168-9002.
[45] M.B. Chadwick and P. G. Young (1996), lANL, USA, ENDF/B-VI evaluation, MAT # 600, revision 2, June 1996, data retrieved from the ENDF database.
[46] K. Wisshak, F. Voss, F. Käppeler, M. Krtička, S. Raman, A. Mengoni, and Gallino, Phys. Rev. C **73** (2006), ISSN 015802.
[47] C. Domingo-Pardo *et al. (The n_TOF Collaboration)*, Phys. Rev. C **74**, 025807 (2006).
[48] F. Corvi, A. Prevignano, H. Liskien, and P. B. Smith, Nucl. Instrum. Methods A **265**, 475 (1988).
[49] F.G. Perey *et al.*, in *Nuclear Data for Science and Technology* (Mito, 1988), p. 379.
[50] R. Macklin, Nuclear Science and Engineering **95**, 200 (1987).
[51] P.E. Koehler *et al.*, Phys. Rev. C **54**, 1463 (1996).
[52] J. N. Wilson, B. Haas, S. Boyer, D. Dassie, G. Barreau, M. Aiche, S. Czajkowski, C. Grosjean, and A. Guiral, Nucl. Instrum. Methods A **511**, 388 (2003), ISSN 0168-9002.
[53] S. Agostinelli *et al. (Geant4 Collaboration)*, Nucl. Instrum. Methods A **506**, 250 (2003).
[54] C. Domingo-Pardo, Ph.D. thesis, CSIC-University of Valencia (2004).
[55] C. Domingo-Pardo *et al. (The n_TOF Collaboration)*, Phys. Rev. C **74**, 055802 (2006).
[56] C. Domingo-Pardo *et al. (The n_TOF Collaboration)*, Phys. Rev. C **75**, 015806 (2007).
[57] C. Domingo-Pardo *et al. (The n_TOF Collaboration)*, Phys. Rev. C **76**, 045805 (2007).
[58] J. L. Tain and D. Cano-Ott, Nucl. Instrum. Methods A **571**, 719 (2007).
[59] J. L. Tain and D. Cano-Ott, Nucl. Instrum. Methods A **571**, 728 (2007).
[60] C. Guerrero, D. Cano-Ott, E. Mendoza, and J. L. Taín, in *Proceedings of the 16th International Conference on Capture γ-ray Spectroscopy and Related topic, Cologne, Germany, 2008*, edited by J. Jolie, A. Zilges, N. Warr, and A. Blazhev (2009), vol. 1090 of *American Institute of Physics Conference Series*, pp. 372–375.
[61] U. Abbondanno *et al. (The n_TOF Collaboration)*, Nucl. Instrum. Methods A **538**, 692 (2005).

[62] S. Marrone *et al.*, Phys. Rev. C **73**, 034604 (2006).